NATIONAL AERONAUTICS AND SPACE ADMINISTRATION

Technical Report 32-1233

Corrosion of Niobium-1% Zirconium Alloy and Yttria by Lithium at High Flow Velocities

L. G. Hays

JET PROPULSION LABORATORY

CALIFORNIA INSTITUTE OF TECHNOLOGY

PASADENA, CALIFORNIA

December 1, 1967

NATIONAL AERONAUTICS AND SPACE ADMINISTRATION

Technical Report 32-1233

Corrosion of Niobium-1% Zirconium Alloy and Yttria by Lithium at High Flow Velocities

L. G. Hays

Approved by:

D. R. Bartz, Manager
Research and Advanced Concepts Section

JET PROPULSION LABORATORY
CALIFORNIA INSTITUTE OF TECHNOLOGY
PASADENA, CALIFORNIA

December 1, 1967

TECHNICAL REPORT 32-1233

Prepared Under Contract No. NAS 7-100
National Aeronautics & Space Administration

Acknowledgment

Loop fabrication and test operations relating to material reported herein were performed under the direction of D. O'Connor and G. M. Haskins. Contributions to the metallurgical and chemical evaluations of materials were provided by R. Moss and S. P. Vango.

Page intentionally left blank

Page intentionally left blank

Contents

Tables

Figures

Contents (contd)

Figures (contd)

Abstract

An experiment was performed to measure the material removal from two materials—niobium-1% zirconium alloy and yttrium oxide—by a lithium stream flowing at a maximum velocity of 48.5 m/s. After 109 hr at 1143°C, the yttria specimens were completely dissolved. After an additional 391 hr at 1073°C, the maximum depth of material removal from the niobium alloy was measured to be about 7 μm. This value corresponds to the depth calculated from turbulent mass-transfer relations for simple dissolution if the temperature coefficient of solubility is taken to be 1.2×10^{-9} g Nb/g Li °C. The measured variation of material loss with lithium velocity follows the dependency predicted by these relations, indicating a diffusion-limited process.

Corrosion of Niobium-1% Zirconium Alloy and Yttria by Lithium at High Flow Velocities

I. Introduction

A liquid-metal magnetohydrodynamic power system for use in space is currently being investigated at the Jet Propulsion Laboratory. In this cycle, lithium in the liquid state is accelerated by cesium vapor in a two-phase nozzle, is then separated from the cesium, decelerated in a magnetohydrodynamic (MHD) generator, and finally forced by its remaining dynamic head through a heat source to the nozzle.

The lithium flowing on the separating surface and in the generator will reach velocities as high as 150 m/s. The corrosive nature of liquid-metal flow at these velocities was an area of concern for this, and many other, liquid-metal power systems, since no applicable corrosion experiments above about 5 to 10 m/s have been reported. If the transport of wall material into the liquid metal is limited by the fluid dynamic processes, then the rate of dissolution in a turbulent flow in a channel should be proportional to the 0.8 power of velocity (Refs. 1 and 2). However, for the case where the process limiting resistance is due to interfacial phenomena between the wall and liquid metal, no definitive relationship between velocity and mass transfer has been established. Moreover, the possibility exists that, as velocity is increased for a particular system of solute and solvent, the limiting mechanism may change from the latter (solution-limited) case to the former (diffusion-limited) case, due to the removal of corrosion products or surface complexes. Thus, data obtained at low velocities may not be meaningful at higher velocities, because of change in the controlling mechanism.

The solvent-solute combination of interest for the liquid-metal magnetohydrodynamic power system is lithium and niobium-1% zirconium (Nb-1% Zr) alloy. This niobium alloy is readily available and possesses good fabricability and adequate strength for the system. Excellent long-term compatibility has been demonstrated by this pair at temperatures to 1100°C, the maximum for this application. In a 10,000-hr test at about 1100°C, no measurable material removal occurred at locations where lithium velocities were in the range of about 3 to 6 m/s (Ref. 3). This result is typical of experience for static, capsule tests and flow systems with low velocities. However, in the same flow system, measurable material loss occurred at a location where the velocity was 12 m/s and, also, at the leading edge of heat exchanger tubes, which experienced impingement by the lithium stream.

In the latter location about 0.2 mm of grain-boundary dissolution occurred. The material loss that was suffered emphasizes the fact that there is a significant fluid-dynamic and velocity effect on mass transfer of even the most compatible liquid-metal structural-material combinations.

To provide data for the liquid-metal magnetohydrodynamic power system, an experiment was designed to measure the material removal from Nb-1% Zr plates by a high-velocity lithium stream. The plates were placed in three locations where the velocity would vary by the ratio of 1:1.75:2.50. In addition, yttrium oxide (Y_2O_3) plates were mounted in adjacent locations to determine their resistance to flowing lithium. Yttria had previously been established to be more compatible with lithium at 1100°C than other ceramic materials by several static capsule tests of 100 to 3000 hr (Ref. 4). The test section was so designed that the results could be compared with analytical predictions of material loss based on simple dissolution with diffusion-limited mass transfer. During the experiment, the maximum temperature was 1143°C, and the maximum velocity at the location of the test plates was 48.5 m/s.

II. Theoretical Considerations

A substantial body of literature exists that indicates the validity of the analogy between heat and mass transfer when applied to liquid-metal flows (e.g., Refs. 1 and 2). Non-liquid-metal heat-transfer relations have been shown to describe liquid-metal mass transfer when the corresponding nondimensional mass-transfer groupings are substituted [i.e., Sherwood number (Sh) for Nusselt number and Schmidt number (Sc) for Prandtl number]. The case of mass transfer of wall material into a fully developed turbulent stream when simple dissolution occurs can be described by the following relation:

$$Sh = 0.023\, Re^{0.8}\, Sc^{0.33} \tag{1}$$

The mass-transfer coefficient k_d is contained in the Sherwood number Sh (see nomenclature). If k_d is determined from Eq. (1) for given flow conditions and fluid properties, then the mass-transfer rate from the wall is:

$$\dot{m}_w = k_d \rho_s (C_w - C_s) \tag{2}$$

For the diffusion-limited case, the concentration at the wall C_w corresponds to the solubility at the wall temperature. The bulk stream concentration C_s varies from one location to another in the test loop because of material that has been added to, or lost from, the flowing stream. The term C_s can also be expressed as the solubility S at some temperature T_c (hereafter referred to as the effective concentration temperature). For small concentration differences, Eq. (2) may then be expressed in terms of the depth of material removal as:

$$\Delta t_w = k_d \frac{\rho_s}{\rho_w} \frac{\partial S}{\partial T}\bigg|_{T_w} (T_w - T_c)\, \tau \tag{3}$$

In order to apply Eq. (3) to predict the depth of material removal from the niobium alloy plates in the test section, the effective concentration temperature T_c must be determined by stepwise application of Eqs. (1) and (2) from some place in the test system where the concentration is known. In the present case, as discussed later, this location is at the outlet of the reservoir. In addition, two properties of the niobium-lithium system are required, which are not well known: the diffusivity D_v and the solubility $S(T)$.

The diffusivity of niobium in lithium can be estimated from the Einstein–Stokes relation, which has provided reasonable agreement with most other solid-metal liquid-metal combinations (Ref. 2).

$$D_v = \frac{kT}{6\pi \mu_s r_a} \tag{4}$$

Attempts have been made to measure the solubility of niobium in lithium. However, the experimental data vary from about 1 to 900 ppm by weight at temperature of ~1000°C (Ref. 5). Therefore, the approach used was to determine the temperature coefficient of solubility *a posteriori* from the best correlation of the experimental data. If the velocity dependence of material loss follows the relationship predicted by these equations, then the process may be identified as diffusion limited rather than solution limited. However, since an empirical fit of solubility coefficient is required, an uncertainty still exists as to whether simple dissolution is occurring or if some more complex, temperature-dependent chemical reactions provide the driving potential for material loss. In either case, an empirical relation results that gives the material loss as a function of temperature difference and flow conditions.

III. Experimental Parameters and Apparatus

The configurations of the niobium alloy and yttria plates and the holder are shown in Fig. 1. The plates formed one wall of the flow channel, while the area (and velocity) variation was provided by passages machined in the

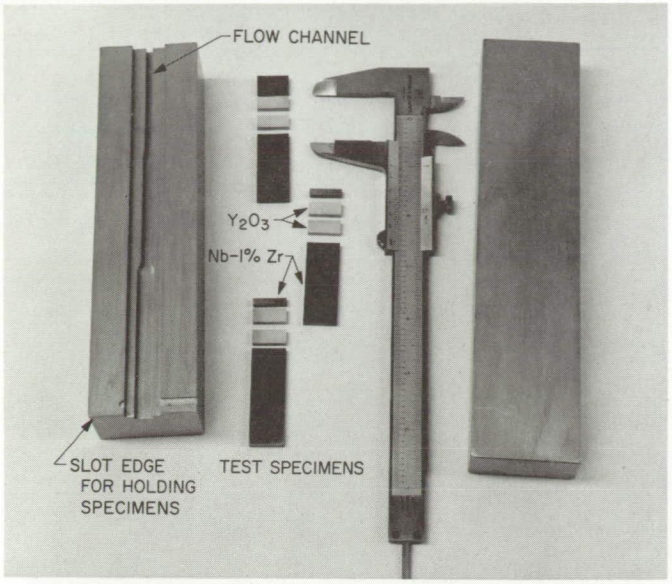

Fig. 1. Lithium test section before welding

Nb-1%Zr holder. The dimensions of the flow passage and corresponding hydraulic diameters are given in Table 1. Rectangular flow passages were chosen so that the test specimens could be flat, providing the greatest accuracy of measurement before, and after, the test. The plates were held in place mechanically and extended outside of the flow channel, enabling direct comparison after the test of exposed and unexposed surfaces.

Table 1. Test section dimensions

Section No.	Height, cm	Width, cm	Length, cm	Hydraulic diameter, cm
1	0.307	0.762	6.00	0.440
2	0.307	0.445	5.21	0.361
3	0.307	0.307	4.66	0.307

A schematic representation of the flow system that provided the high-velocity, high-temperature lithium in the test section is given by Fig. 2. The lithium was pressurized and heated in an electromagnetic induction pump with a helical Nb-1%Zr duct and flowed at moderate velocity through an electromagnetic flowmeter to the test section, where acceleration to higher velocities occurred. The lithium stream discharged from the test section at high velocity into a reservoir, dissipating most of the thermal and kinetic energy added by the pump. The flow exited from the reservoir through a filter and was returned through another flowmeter to the pump. The large surface area and highly turbulent flow in the reservoir-filter

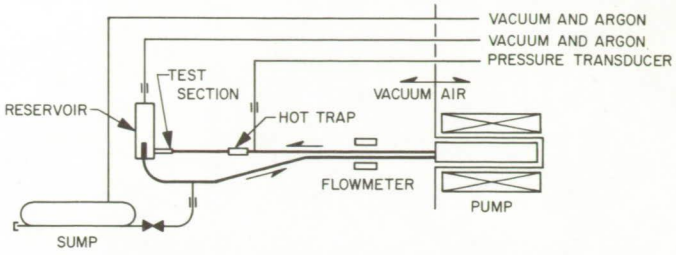

Fig. 2. High-velocity lithium flow system

should have caused saturation to be reached at this location. This conclusion was verified by extensive deposits found in the reservoir after the tests were completed.

The primary flow circuit of the test system was fabricated of Nb-1%Zr alloy and was operated within a vacuum chamber. External connections of stainless-steel auxiliary lines to the test system were made through unions formed by coextrusion of the niobium and stainless-steel alloys. The niobium alloy duct of the electromagnetic pump was contained within the vacuum environment by a thin-wall, stainless-steel sleeve. A three-phase motor stator on the outside of the sleeve provided the electromagnetic body forces to the lithium within the duct. All heat input to the lithium resulted from eddy-current losses from the pump.

The test loop was sized so that the radiant-energy losses at about 1100°C to the vacuum-chamber wall, which was at 260°C, would balance the energy input from the pump. The vacuum-chamber walls were maintained at this temperature during the test to keep the lithium in ancillary lines molten. Figure 3 shows the test section, reservoir, and return line during operation at elevated temperature. A more detailed description of the experimental apparatus is furnished in Appendix A.

The test system was operated for two periods at constant temperature. The first of these periods lasted 109 hr and the temperature was maintained at 1143°C. The mass flowrate was 0.202 kg/s, yielding a maximum velocity of 48.5 m/s. The testing was discontinued when the filter at the reservoir exit collapsed, resulting in a restriction of the flow and cavitation in the pump. The test section was removed, and examination revealed complete dissolution of the yttria plates to have occurred. Complete dissolution of yttrium metal in an upstream hot trap had also taken place. The filter was replaced by one of improved design, the upstream hot trap was deleted, and the test section and piping were reinstalled. After 391 hr of operation at 1073°C, the 500-hr high-temperature test was completed.

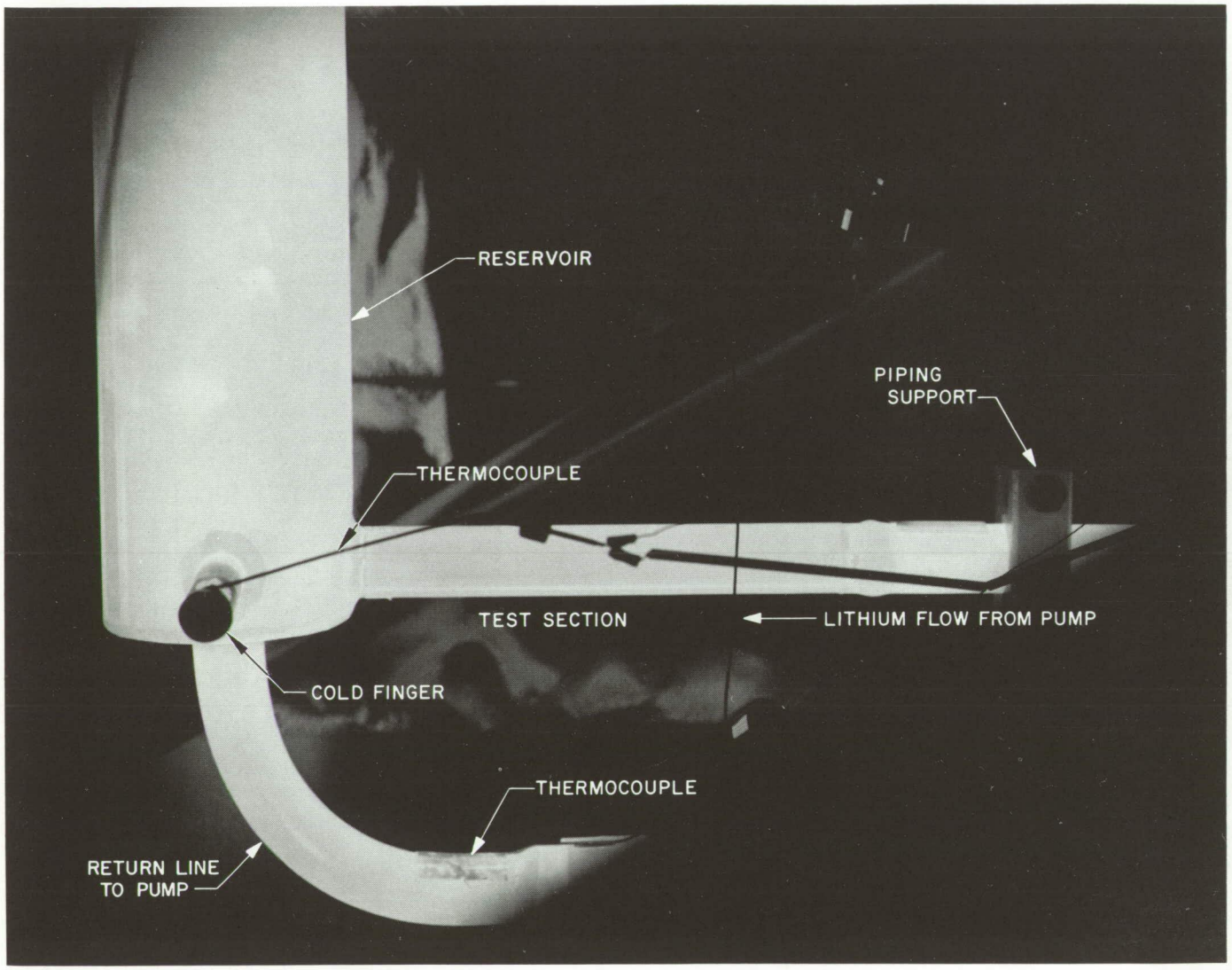

Fig. 3. Lithium test section and reservoir during operation at elevated temperature

All materials were representative of purity levels required for a space power system. Analyses of the lithium, niobium alloy, and yttria—both before and after testing—are given in Table 2. The oxygen analysis on the lithium was performed by neutron activation techniques, while spectrographic and chemical tests were performed to measure the other elements. The most significant result is the large increase in total oxygen content experienced by the lithium, resulting from dissolution of yttria. After 109 hr, the oxygen increased to 0.140% from the initial value of 0.0382%. After replacing part of the lithium and operating for an additional 391 hr, the percentage had decreased to between 0.049 and 0.047%. While this amount of oxygen is relatively large, most of it is probably inactive because of the large amount of yttrium in solution.

Table 2. Analyses of test materials

Material	Content, wt %	
	Pretest	Post-test
Lithium		
O	0.0382	0.140,[a] 0.049, 0.047
N	<0.006	0.002
C	<0.001	<0.001
H	0.0056	0.0021
Nb	—	<0.02
Y	<0.02	<0.02
Pb	<0.01	<0.01
Mg	0.00037	0.00061, 0.00058
Fe	0.0014	<0.001, 0.00081
Cu	0.00013	0.00010, 0.00076
Al	0.0014	0.00026
Cr	<0.0002	<0.0002
Ca	0.0077	0.0067, 0.0049
Li	remainder	remainder
Other elements	nil	nil
Niobium-1% Zirconium		
H	0.00025	0.00023, 0.0004
C	0.0090	0.0081
O	0.0140	0.009
N	0.0070	0.004
Yttrium oxide		
C	0.025	—
N	0.006	—
Si	0.009	—
O	20.0	—

[a]After 109 hr. All other values after 500 hr.

IV. Experimental Results

The macroscopic appearance of the niobium alloy test specimens after 500 hr at temperatures above 1073°C are shown by Figs. 4 and 5. These pictures reveal several changes to have occurred.

(1) A crystalline deposit was formed in the flow channel.

(2) Material removal was minor in the high-velocity, fully developed flow regions.

(3) Material removal was heavy from the niobium alloy downstream of a cavity left by dissolved yttria. This apparently resulted from local cavitation due to the sharp corner.

(4) Moderately heavy cracking due to hydrogen embrittlement occurred on all surfaces exposed to lithium as a result of post-test removal treatment with water.

The deposit was identified by chemical analysis to be yttrium. These crystals appear to have formed during the 10-hr cooling period after the test was completed from the yttrium previously dissolved in the lithium. Since the lithium was saturated with yttrium at the test temperature, slow cooling of the lithium while maintaining flow resulted in crystal formation on the wall at the high-velocity location. This conclusion is supported by observation that the grooving of the substrate surface, discussed below, was continuous from underneath the crystals to locations where no crystal was formed.

Deposits of crystalline material were formed in the reservoir. Spectrographic analysis of these deposits revealed their major constituents to be zirconium, yttrium, and niobium. (A trace amount of copper was found, also.)

Measurable material removal, although slight, occurred in the fully developed flow regions. Figure 6 is a photomicrograph showing the typical appearance of the surfaces in the flow channel and of the surfaces immediately adjacent to the flow channel (where seepage, but little post-test deposition, occurred). Additional photomicrographs are given in Appendix B, which also show the yttrium deposits. The most striking characteristic of these surfaces is the pronounced grain-boundary grooving for crystal planes intersecting the surface. The direction of the grooves were completely independent of the direction of flow. The surface had no post-test metallurgical preparation, so the grooving resulted from the preferential dissolution at these locations by lithium.

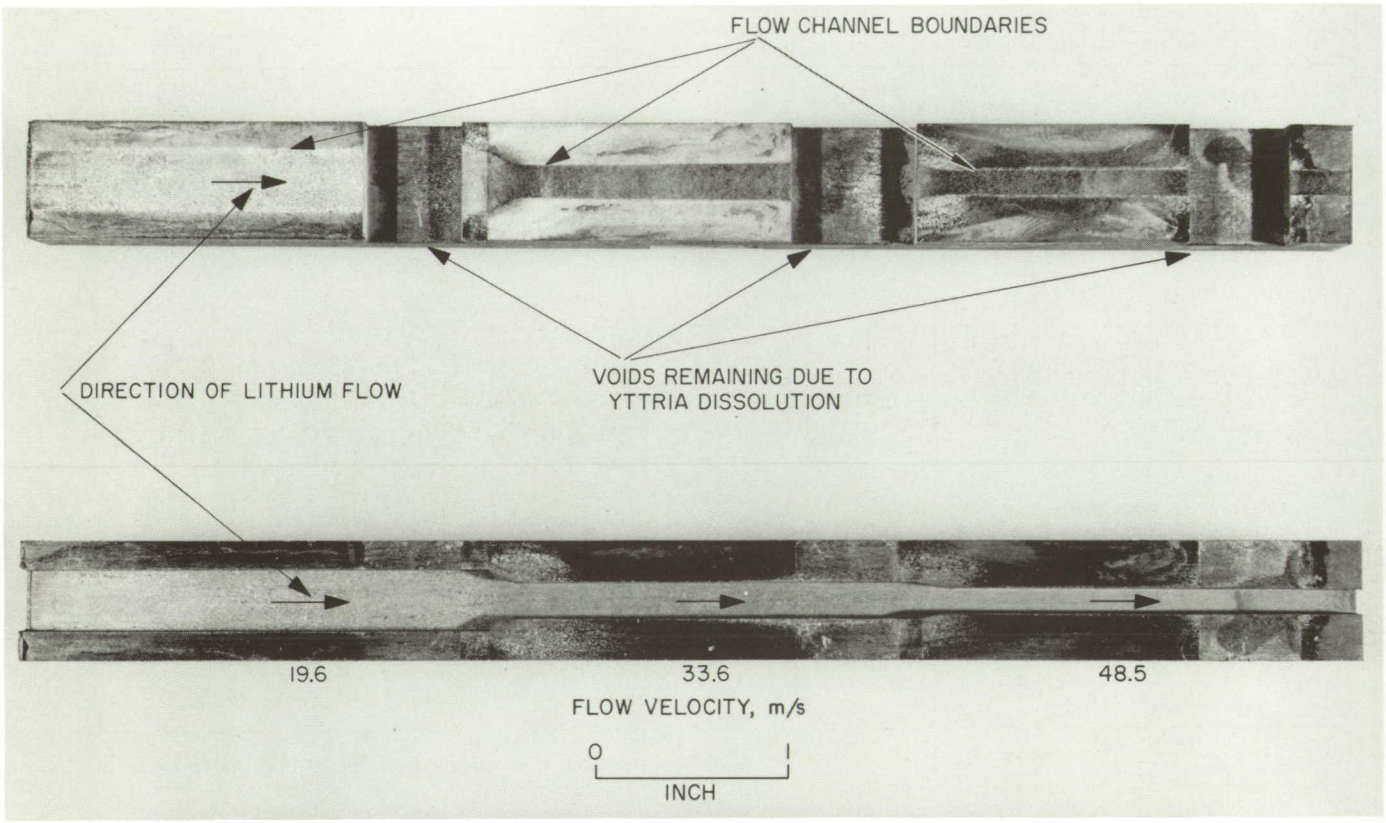

Fig. 4. Lithium test section after 500-hr flow at 1073–1143°C

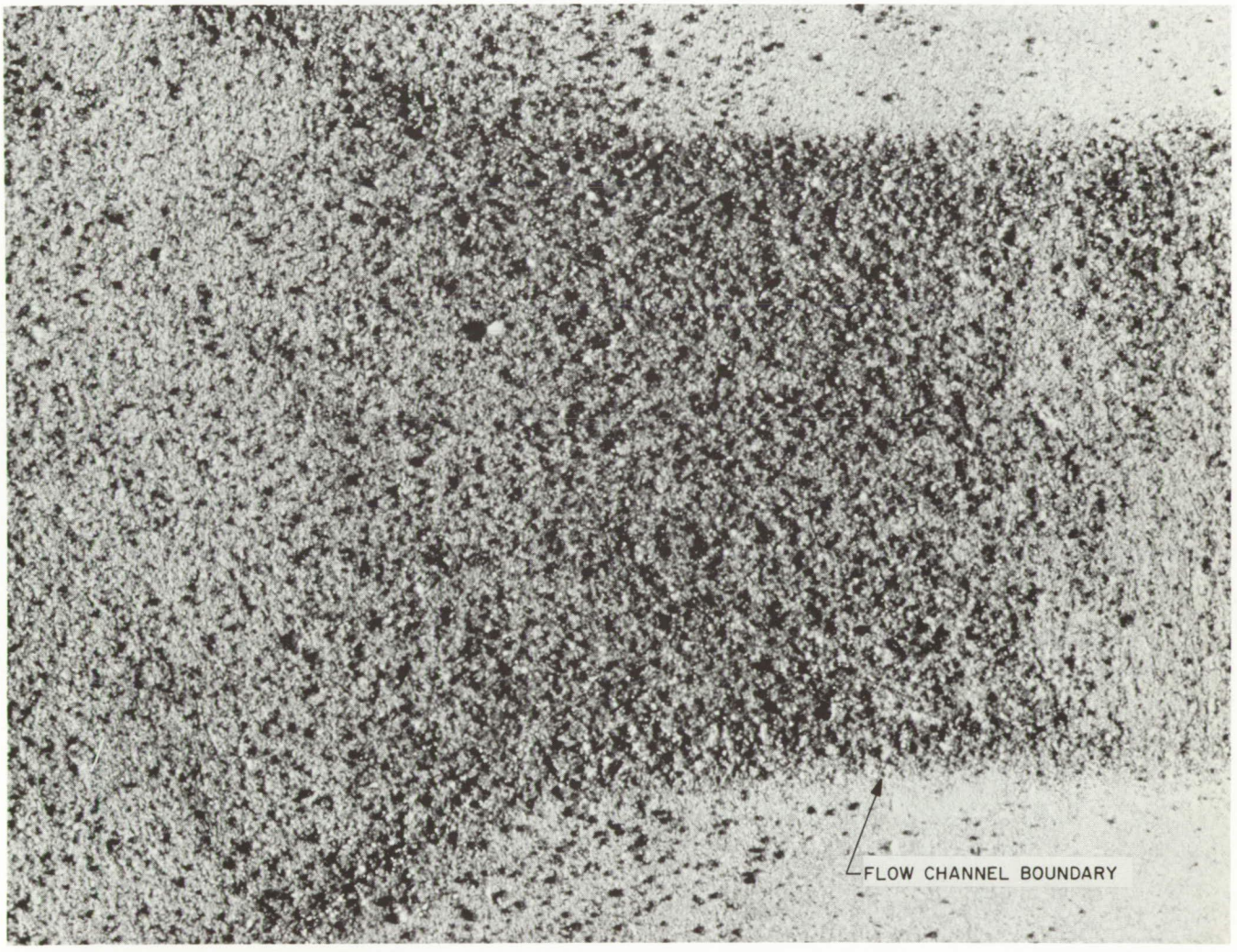

Fig. 5. Surface of lithium flow channel after 500 hr at 1073–1143°C (0.44-cm width) (Photo reduced to 75%)

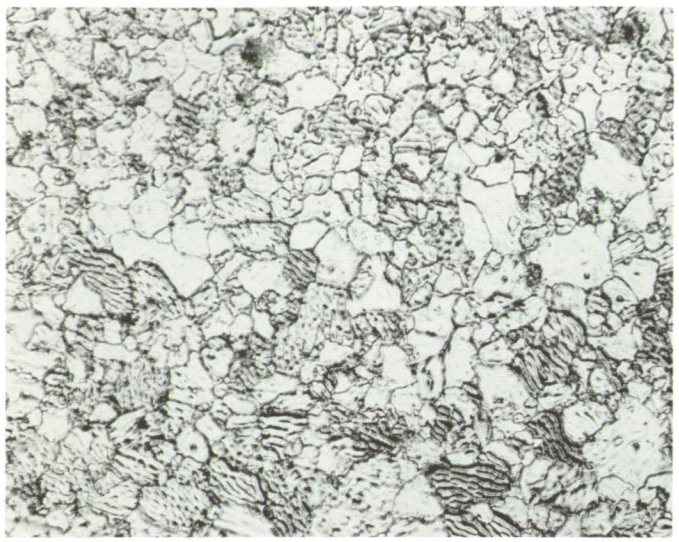

Fig. 6. Surface of lithium flow channel after 500 hr at 1073–1143°C (250 ×) (Photo reduced to 82%)

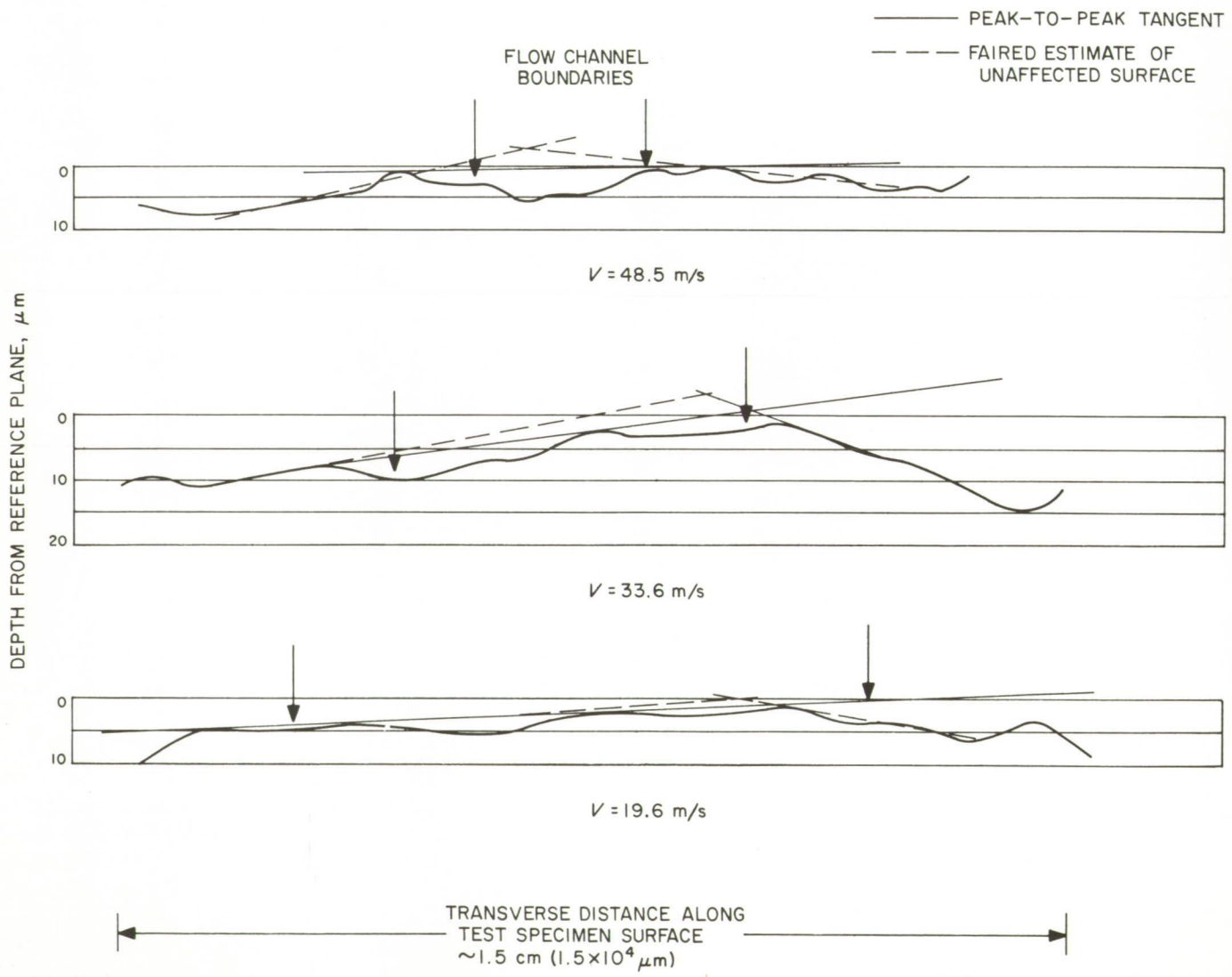

Fig. 7. Profiles of test section surface at $x/d_h = 10$ after 500-hr lithium flow at 1073–1143°C

Traverses of the surfaces at the location for fully developed flow were made with a microscope with a calibrated vernier-focusing mechanism. Divisions on the scale were in 2-μm increments and repeatability was within about ½ μm with the approach from a consistent direction. The results of measurements on the niobium alloy are shown in Fig. 7 for the three different regions of flow velocity. The arrows define the limits of the flow region.

Two extremes of material loss were estimated, as illustrated in Fig. 7. One method was to measure the distance between the peak-to-peak tangent and the lowest valley in the flow channel. The other method was to fair a line through the surfaces outside of the flow region and measure the maximum valley depth below that line. The results of these measurements are plotted in Fig. 8 as a function of velocity. The calculated curve (see Appendix C) is shown for comparison. The most important finding is that the highest velocity test specimen exhibited a maximum material loss rate that corresponds to a very small value of solubility. The temperature coefficient of solubility that provides the closest agreement with test data is $\partial S/\partial T = (1.2 \times 10^{-9})$ (g Nb/g Li °C). This value would result from solubilities in the 2 to 3 ppm (by weight) range at 1100°C for a reasonable heat of solution (see Ref. 5). The dependency of the data on velocity is in reasonable agreement with the theoretical variation. The maximum deviation of measured material loss from the curve calculated for the above value of $\partial S/\partial T$ is about 30%. For the range 1070 to 1150°C, if Eq. (4) for diffusivity is used, a preliminary empirical relation for mass transfer based on these test data is

$$\Delta t_w \approx 1.2 \times 10^{-9} k_d \frac{\rho_s}{\rho_w} (T_w - T_c)\,\tau \qquad (5)$$

Application of Eq. (5) can be illustrated by consideration of the 10,000-hr operation of a 300-kWe liquid MHD system with a maximum velocity of 150 m/s. The maximum likely temperature difference in the high-velocity region would be on the order of 2°C. Since the flow rate would be approximately 80 kg/s, this temperature difference represents heat loss and kinetic losses of 480 kWt from the lithium stream, the most likely to be encountered. For this example, the hydraulic diameter at the high-velocity location is 0.38 cm, giving a channel Reynolds number of 1.7×10^6. The Sherwood number is, therefore, 4.4×10^3, and the mass-transfer coefficient is $k_d = 4.8$ cm/s.

Substitution of these values in Eq. (5) gives $\Delta t_w \approx$ 0.022 cm. This loss (or deposit thickness) is within acceptable limits, since the wall thickness and minimum channel opening can be several times as great. Further studies have been initiated to determine more accurately the temperature and velocity history of the lithium in a 300-kWe liquid MHD system. It is probable that the effective temperature difference will be less than 2°C, giving a correspondingly smaller mass-transfer value.

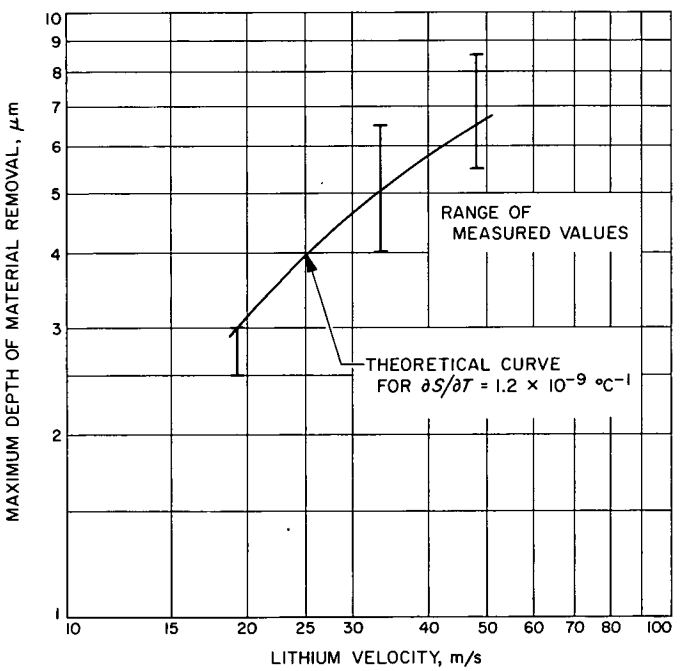

Fig. 8. Depth of material removal from Nb-1% Zr vs lithium velocity, 500 hr at 1073–1143°C

V. Conclusions

High-velocity flow of lithium at a temperature range of from 1073 to 1143°C resulted in complete dissolution of yttrium oxide after 109 hr and in slight dissolution of niobium-1% zirconium alloy after 500 hr. The complete dissolution of yttria test specimens after 109 hr showed this material (which was the most resistant ceramic in static lithium-corrosion tests) to be unsuitable for use with high-velocity lithium. The amount of material removal from the niobium alloy corresponded to that which would be predicted from the equations for diffusion-limited mass transfer, by use of a value for the temperature coefficient of solubility of 1.2×10^{-9} °C^{-1}. The measured velocity dependence of material loss follows the predicted variation. Therefore, the use of mass-transfer relations based on a diffusion-limited mechanism to extend the test results to a wider range of variables appears valid. Application of these test data to an example of a liquid-metal magnetohydrodynamic space-power system shows the maximum mass transfer in 10,000 hr to be within acceptable limits.

Appendix A
Experimental Apparatus

I. Vacuum Containment System

The niobium-1% zirconium flow loop required a vacuum environment for operation in the temperature range of the test (1073 to 1143°C). This requirement was met by the containment system shown in Fig. A-1. The stainless-steel vacuum chamber, which was about 1½ m in diameter by 2 m in length, was traced with electrical heaters and cooling passages and lagged with fiberglass insulation. The heaters were used for bakeout at temperatures to 350 to 450°C. The cooling passages were used for heat removal when the experiment was at its operating temperature, rejecting about 14 to 16 kW to the vacuum-chamber walls. All ports for feedthroughs, viewing windows, and instrumentation were sealed with copper gaskets. The main door was sealed with a Viton-A O-ring which was water-cooled during bakeout and high-temperature operation.

Pumping was accomplished with a getter-ion pump with a capacity of 1000 l/s. An oil diffusion pump with air-cooled and liquid-nitrogen-cooled baffles was used for pumping in the 10^{-4} to 10^{-5} torr range and for standby. The steady-state pressure of the system, which was reached during the second test period, was about 6×10^{-8} torr. The pressure history during this period is shown in Fig. A-2. Previous qualitative measurements with a gas analyzer showed the major gaseous constituent during

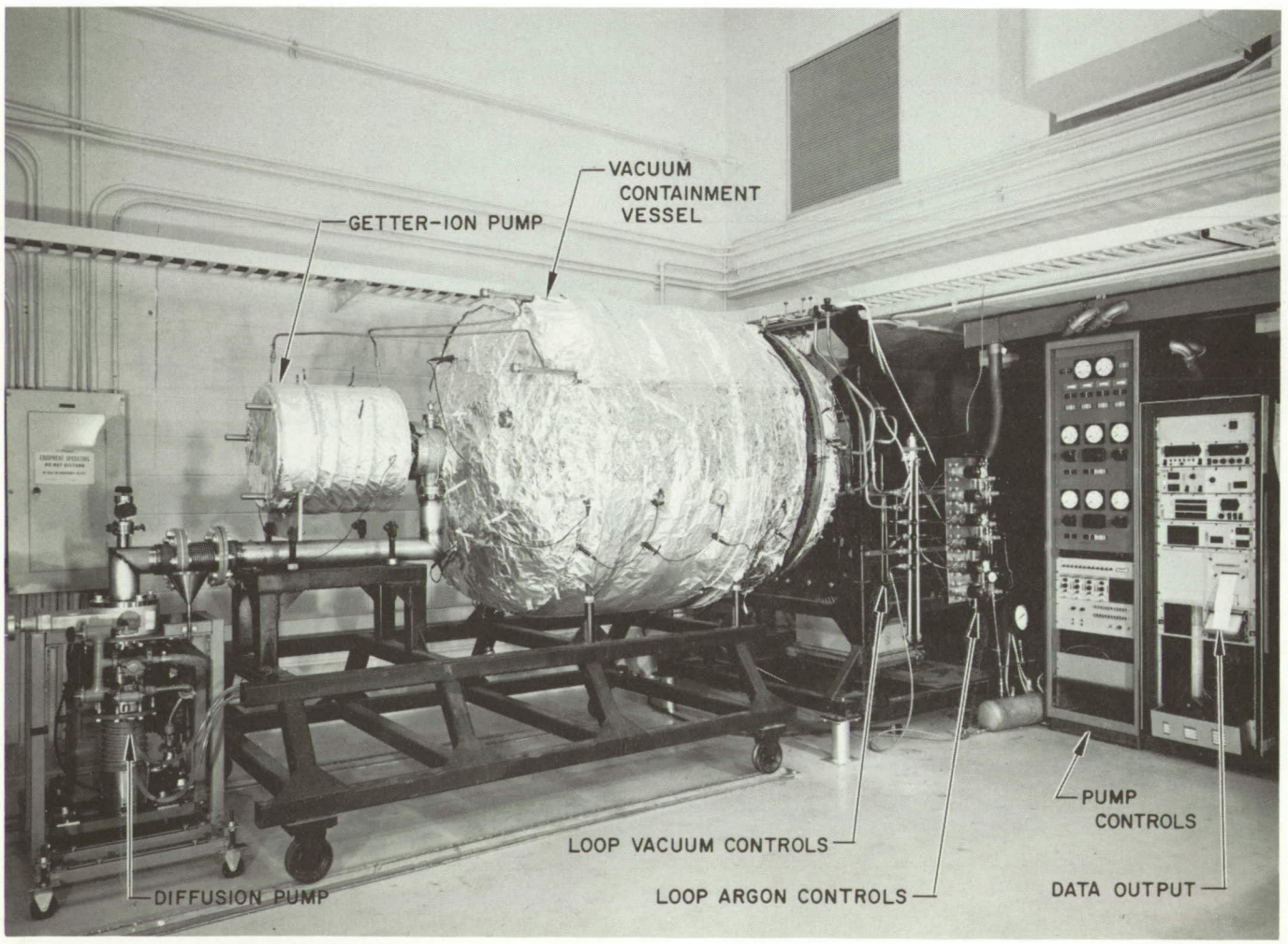

Fig. A-1. Vacuum containment system and controls for high-velocity lithium corrosion experiment

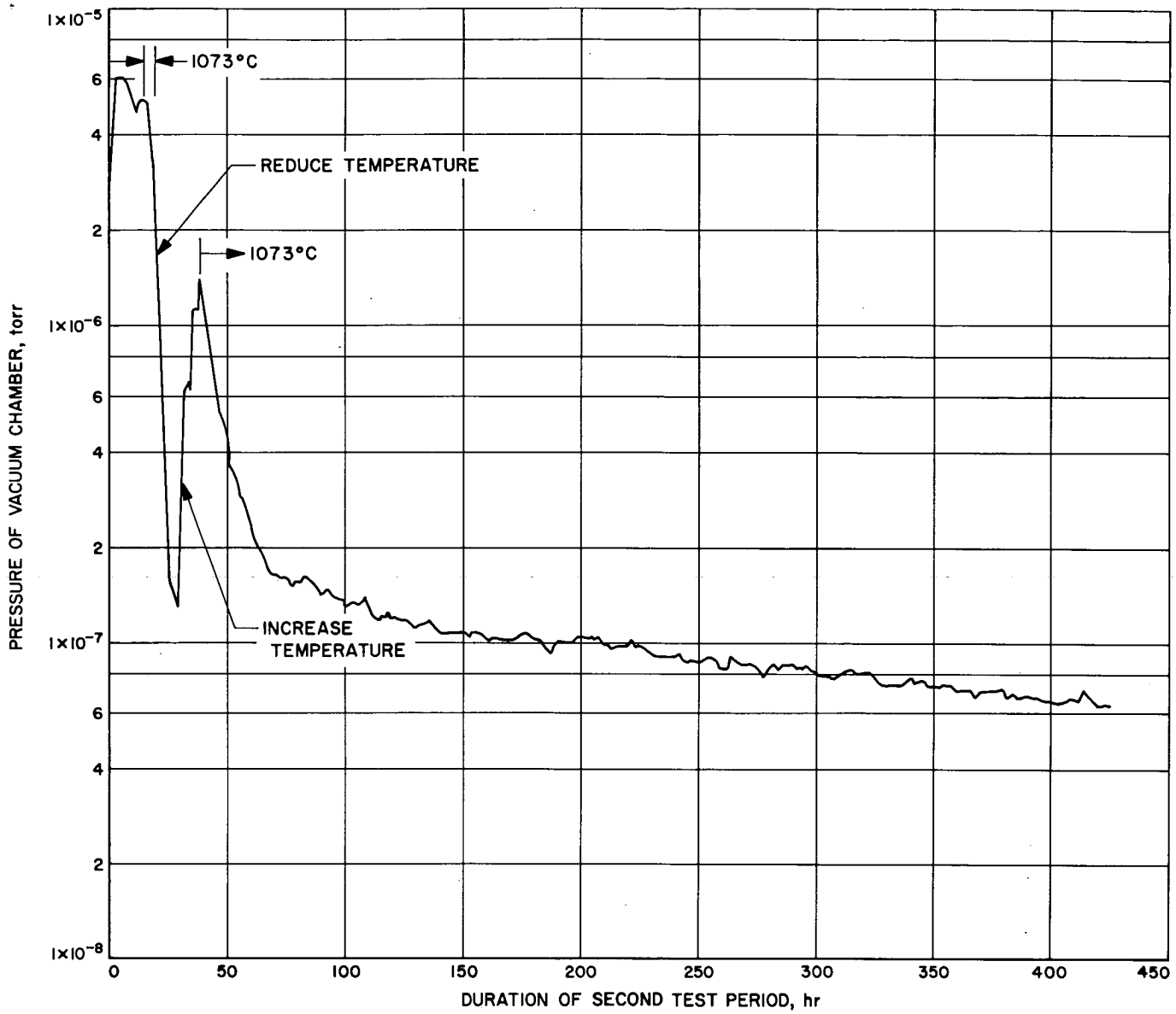

Fig. A-2. Pressure history of vacuum chamber during second test period

the initial outgassing to be hydrogen, liberated from the niobium alloy.

II. Test Loop Assembly

The Nb-1% Zr test loop and auxiliary lines were mounted on the door of the vacuum chamber as shown in Fig. A-3. All external vacuum, argon, and instrumentation connections were provided through the door. The insulation and trace heaters on the sump were used for lithium transfer and were removed before the vacuum-chamber body was mated to the door. During the test, lithium in the auxiliary lines was kept molten by maintaining the vacuum-chamber walls at about 260°C.

More than 20 niobium weldments were required for the final assembly. Most of these welds were performed either in an inert-gas weld chamber or by electron-beam methods. The final joining operations were conducted under an inert-gas cover provided by a lucite enclosure. Contrary to accepted practice, the weldments did not receive an anneal before contact with lithium. However, a satisfactory degree of weld purity was evidently attained, since there was no lithium penetration or weepage during the test period.

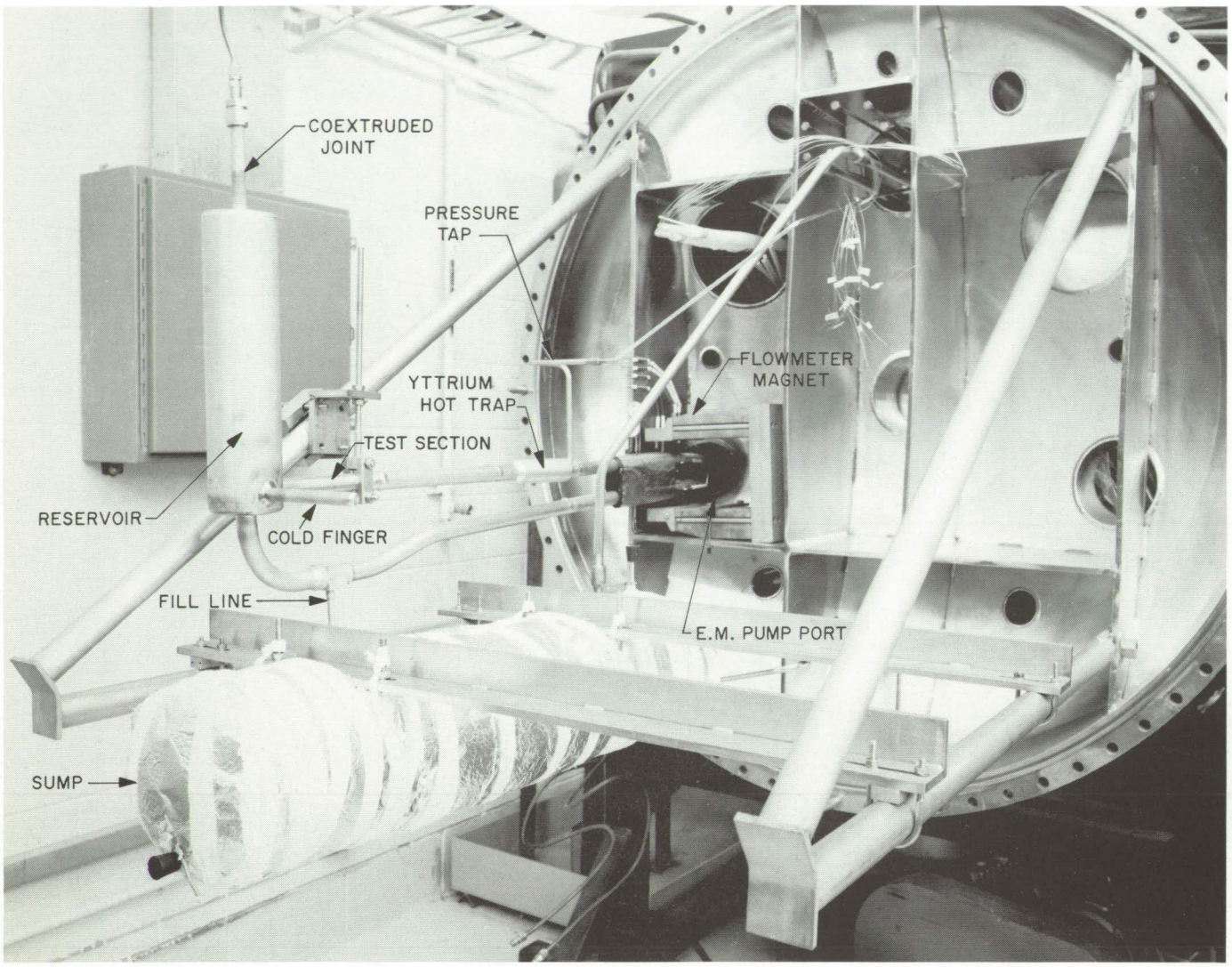

Fig. A-3. High-velocity lithium corrosion test loop before operation

Support for the main piping circuit and components was provided by a sliding block assembly fabricated from molybdenum. This hanger and the port for the pump duct maintained a fixed, vertical position, while allowing lateral displacement.

III. Flow Components

A. Lithium Pump

The lithium pump used for this test was an electromagnetic induction type.[1] The electromagnetic body forces on the lithium were provided by a three-phase stator that was external to the vacuum chamber. This stator is shown installed on the vacuum-chamber door in Fig. A-4. The pump duct, constructed of Nb-1%Zr, was supported by radiation shielding in a stainless-steel sleeve (shown in Fig. A-5), which served as an extension of the vacuum chamber. This sleeve was positioned inside of the stator in the location that would be occupied by the rotor in a motor. The lithium was constrained to follow a helical flow path by the duct, which is shown in Fig. A-6.

The manufacturer's performance curves for this pump at 1100°C had previously been confirmed during the course of a lithium-erosion test (Ref. A-1). These results are shown in Fig. A-7. The pump output was very stable and controllable during both tests. During this test the pump output was held at 20 atm at a flowrate of 0.202 kg/s. This was attained by maintaining the input voltage at 363 V for the duration of the test run.

[1]Manufactured by General Electric Co., Schenectady, New York.

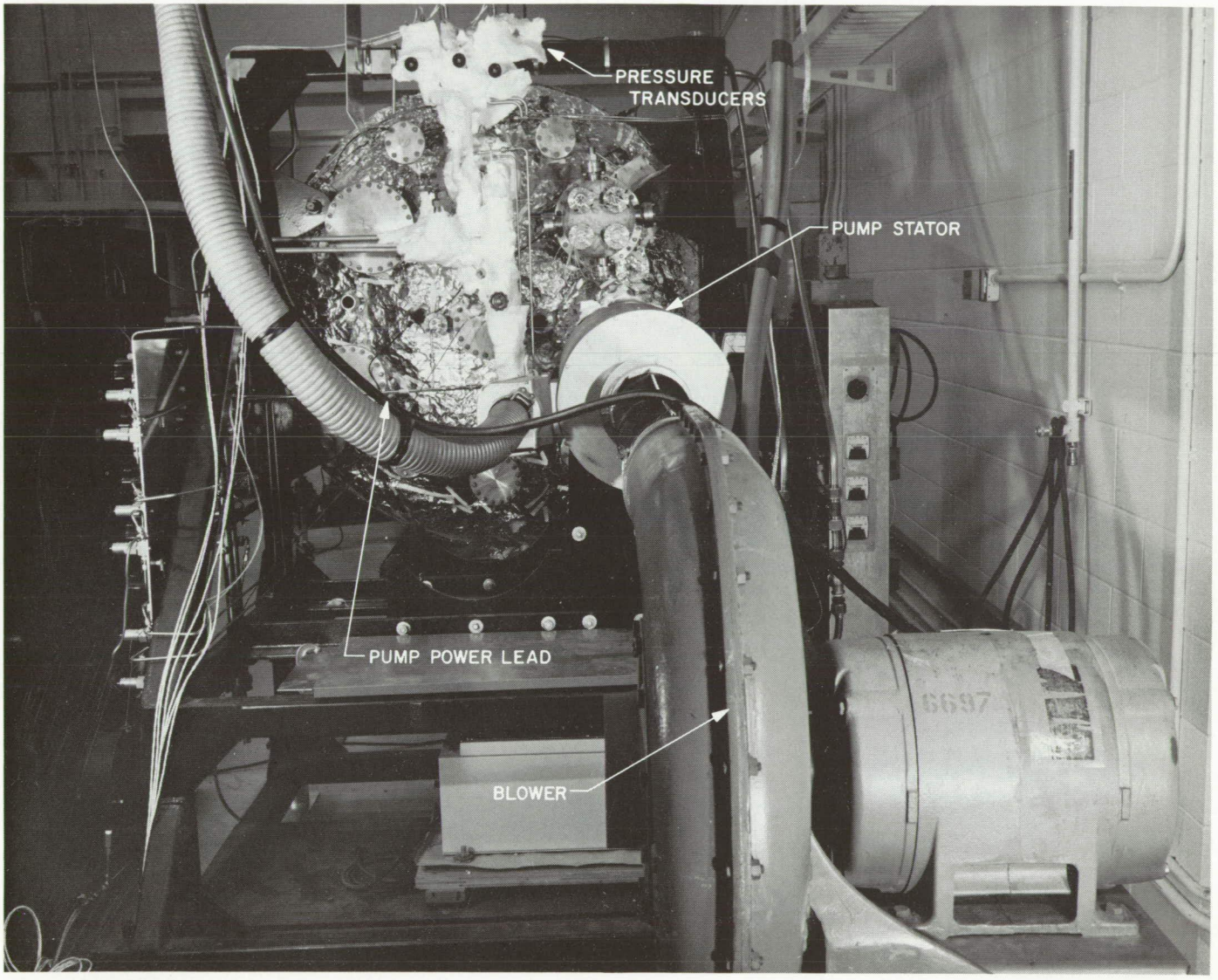

Fig. A-4. Lithium pump installed on door of vacuum chamber

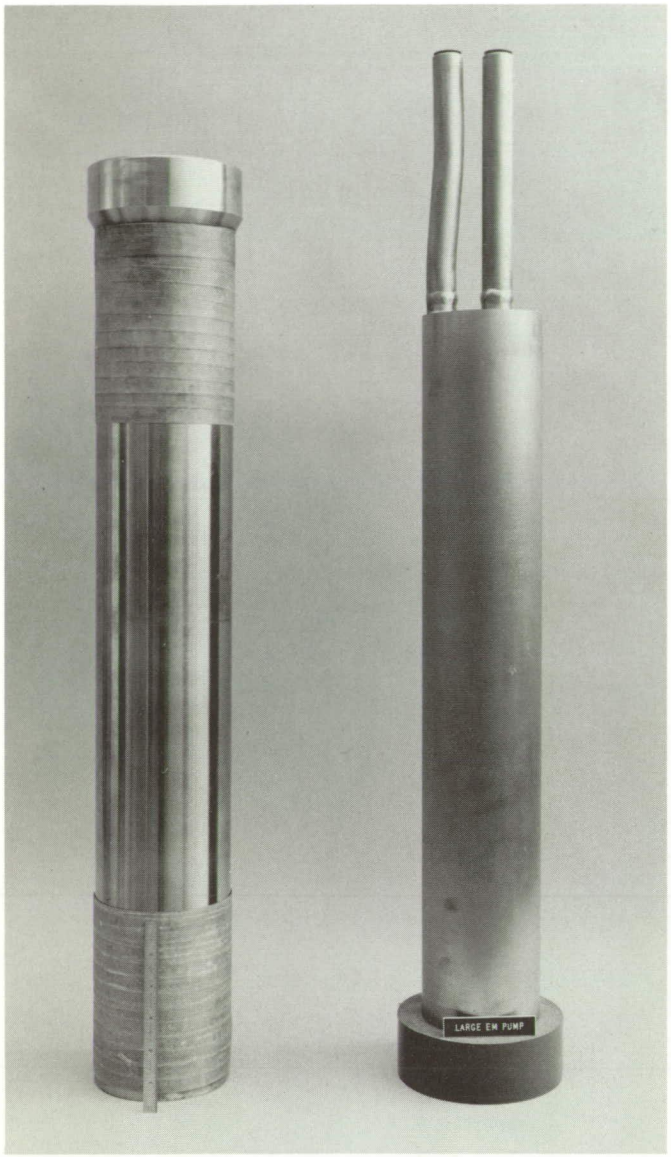

Fig. A-5. Lithium pump duct and insulation assembly

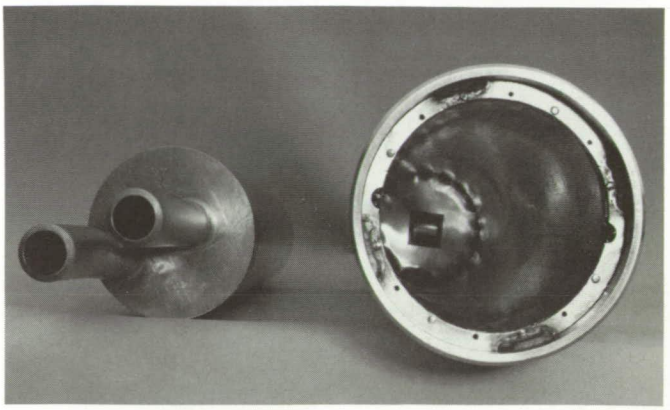

Fig. A-6. Interior of insulation assembly for lithium pump

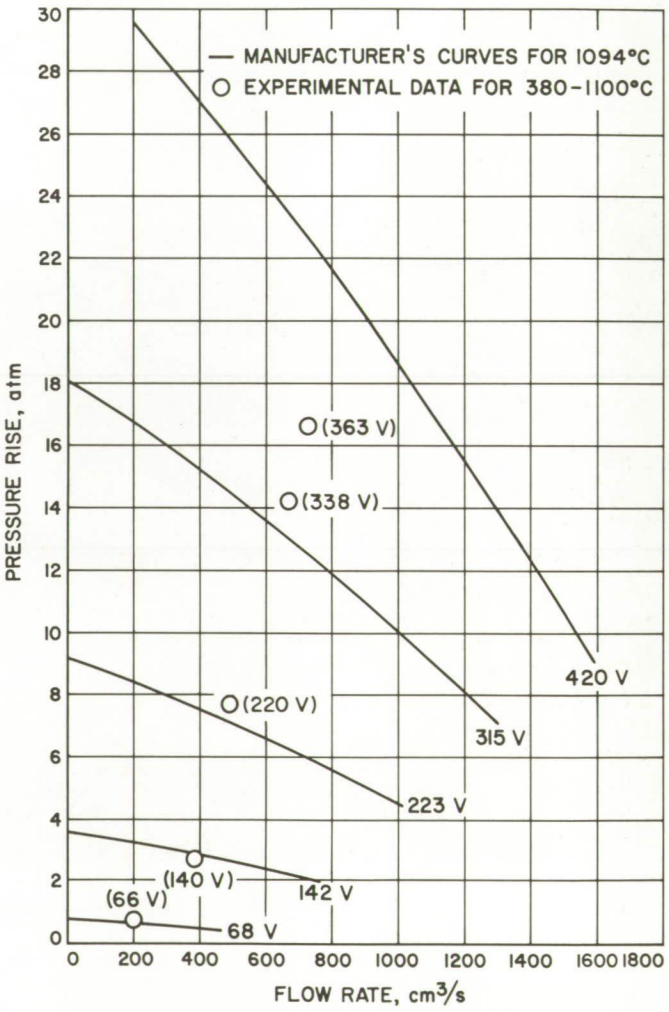

Fig. A-7. Performance of lithium pump

B. Flowmeter

The flowmeter was an electromagnetic, permanent-magnet type.[2] The permanent magnet temperature was maintained at less than 430°C by 20 layers of radiation shielding constructed with a dimpled niobium foil. The calibration of this component (Fig. A-8) was previously compared with simultaneous measurements from flow nozzles with the results shown in Fig. A-9. An identical flowmeter was constructed for this test to provide redundancy for this important measurement. During the 109-hr segment, the two flowmeters read an average of 0.202 kg/s with a total deviation of ± 0.014 kg/s. During the 391-hr period, only one flowmeter was operative. It gave a reading at the end of this period of 0.202 kg/s.

[2]Manufactured by MSA Research Corp., Callery, Penn.

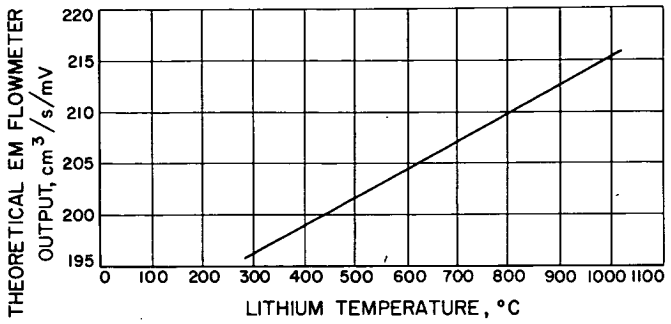

Fig. A-8. Theoretical electromagnetic flowmeter output

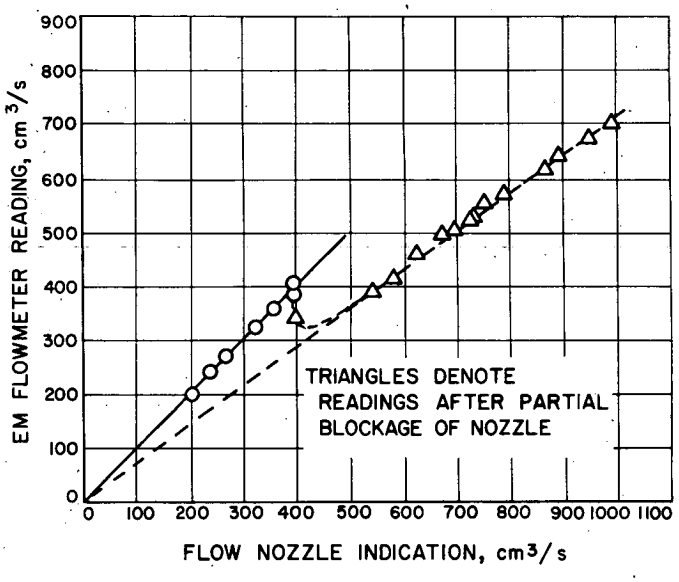

Fig. A-9. Electromagnetic flowmeter calibration

C. Instrumentation

The temperature of the circulating lithium was measured by an optical pyrometer of the disappearing-filament type. During the first test period, the surface of the niobium alloy test section was the target. During the second test period, two hohlraums with a length-to-diameter ratio of 2 were provided to reduce the uncertainty in the measurement. At 1100°C, the pyrometer agreed with a tungsten lamp traceable to the National Bureau of Standards to within ±4°C. Surface thermocouples with radiation shielding were also provided, but errors in the installation procedures resulted in readings which were 50 to 100°C below the pyrometer readings.

The apparent emissivity of the reservoir surface (0.40 from Ref. A-2), pyrex window (0.93), and lucite shield (0.87) combination was 0.32 at a wavelength of 0.65 μm. The corrections for the pyrex window and lucite shield were determined experimentally during the test. The actual reading during the first 109 hr was 1041°C ±2°C. The correction at this emissivity and temperature is 102°C, giving an estimated true temperature of 1143°C, ±2°C. The apparent emissivity of the hohlraum (0.96) and pyrex window combination was 0.892 at a wavelength of 0.65 μm. The actual reading of the pyrometer during the 391-hr period was 1063°C ±1°C. The correction at this temperature for an emissivity of 0.89 is 10°C, giving a true temperature of 1073°C, ±1°C. Figure A-10 shows the reservoir and test section at 1073°C during the 391-hr period, with the hohlraums in the locations indicated.

Pressure transducers of the bonded strain-gage type[3] were used to record the upstream pressure and reservoir pressure. Flow restriction from filters at the reservoir outlet and upstream hot trap (during the first test) prevented meaningful differential measurements. Instead, these readings were used to ensure that the upper limit on pump pressure of 20.4 atm was not exceeded. Installation of these units can be seen in Fig. A-4.

[3]Manufactured by Statham Inst. Co., Los Angeles, Calif.

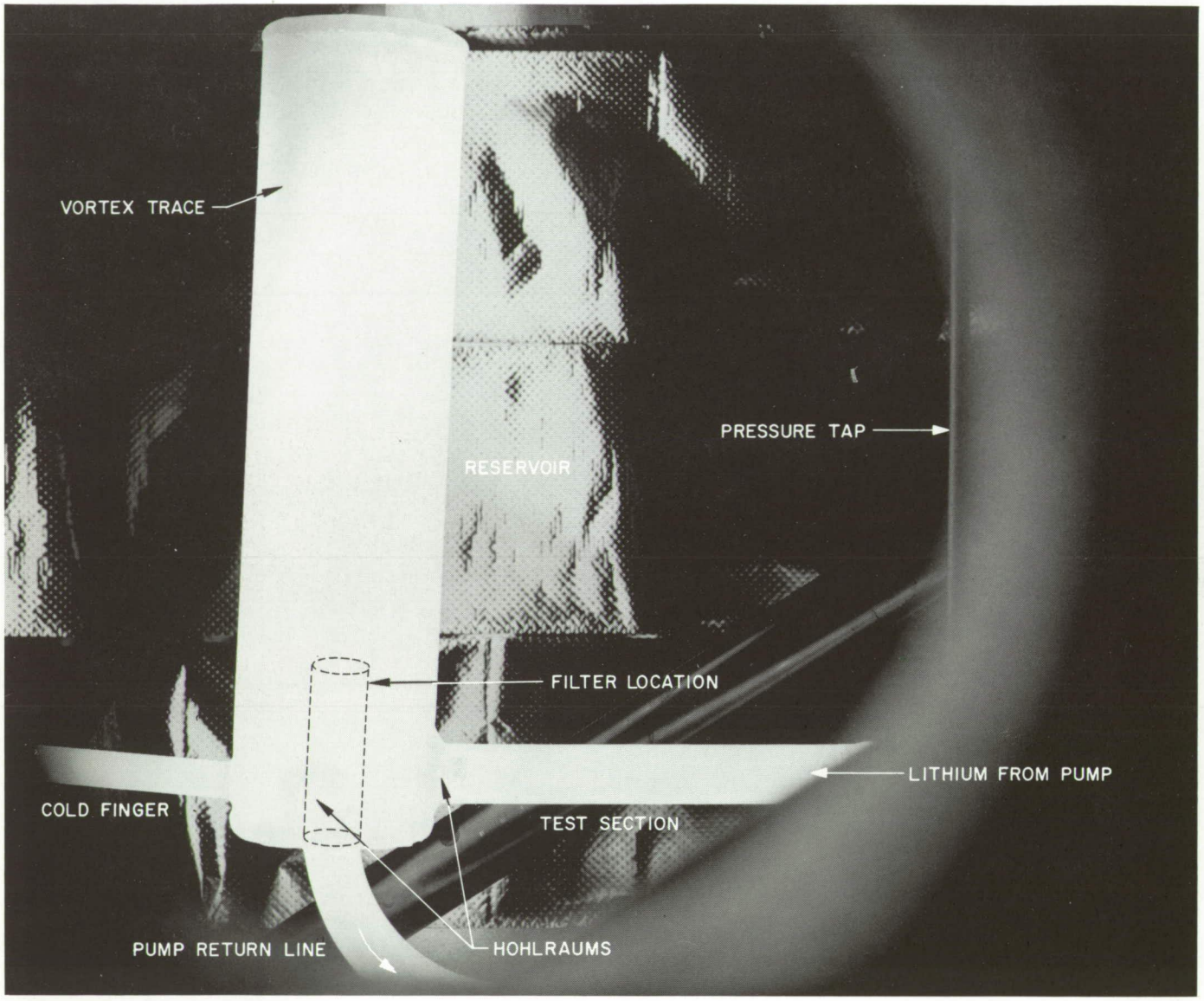

Fig. A-10. Lithium test section and reservoir during operation at 1073°C

Appendix B
Photographic Examination of Materials

I. Structural Portions of Test Loop

The niobium-1% zirconium test loop provided complete containment of the lithium for the 500-hr duration of high-temperature testing. No measurable lithium penetration occurred in welds, in spite of the fact that no post-weld annealing treatment was used. Moderate grain-growth was experienced by the main piping, as shown in Figs. B-1 and B-2. A structure typical of wrought tubing is superimposed on the recrystallized grains in Fig. B-1 from the presence of an impurity (probably carbon). Deletion of this impurity is seen to have occurred from both the outer (vacuum) boundary and the inner (lithium) boundaries. The size of grains at the surface exposed to lithium is larger than that of those in the remainder of the material.

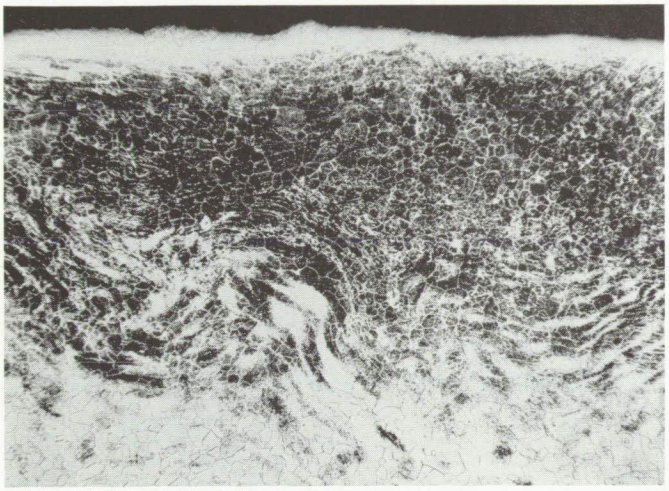

Fig. B-1. Outer diameter of niobium alloy piping after 500 hr at 1073–1143°C (Photo reduced to 75%)

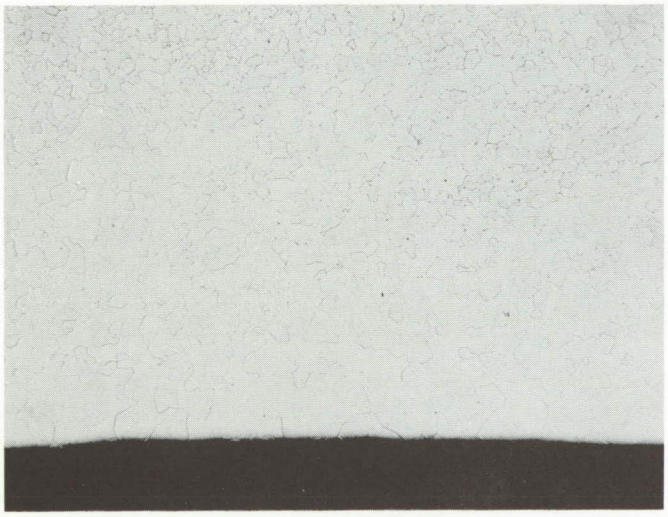

Fig. B-2. Inner diameter of niobium alloy piping after 500 hr at 1073–1143°C (Photo reduced to 75%)

Grooving was observed in welds exposed to the lithium. Figure B-3 is a photograph of a section taken at a weld in the reservoir base. This effect was probably a result of the segregation of oxygen at these boundaries during welding.

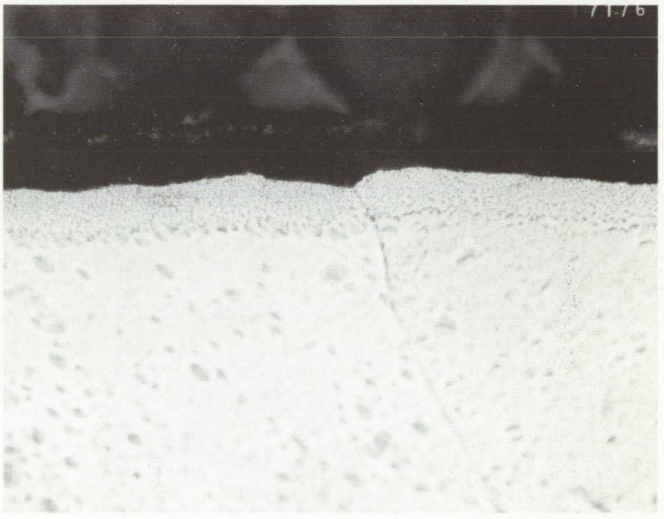

Fig. B-3. Typical grain-boundary grooving in reservoir base plate (Photo reduced to 75%)

A feature of the post-test removal of lithium by water reaction was the embrittlement and cracking of the niobium alloy. This phenomenon which has been reported elsewhere (Ref. B-1) is shown in Figs. B-4 and B-5. The cracking was transgranular in nature and was readily discernable from other material effects produced by the high-velocity lithium. The photographs shown are of the reservoir base plate. Similar cracking, although less severe, occurred in the test section and flow sections of piping that had lithium removed by water reaction.

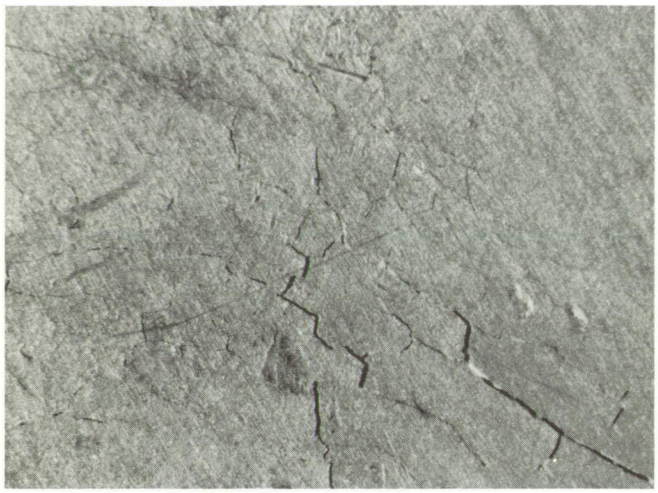

Fig. B-4. Surface cracking in reservoir base plate resulting from post-test removal of lithium by water (Photo reduced to 75%)

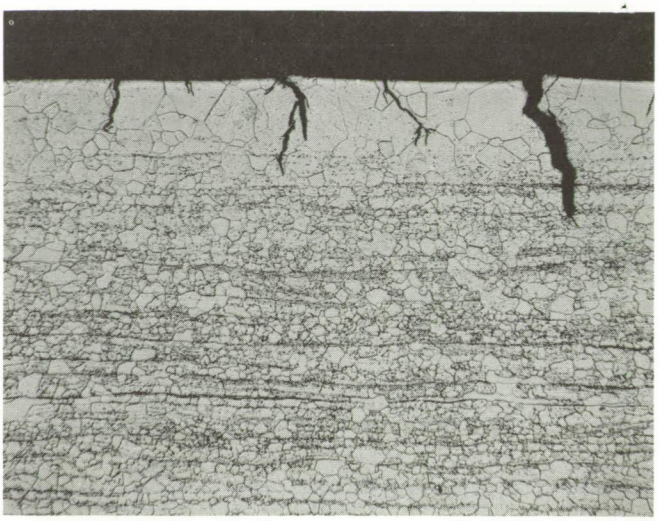

Fig. B-5. Section of reservoir base plate showing surface cracks resulting from post-test removal of lithium by water (100 ×) (Photo reduced to 75%)

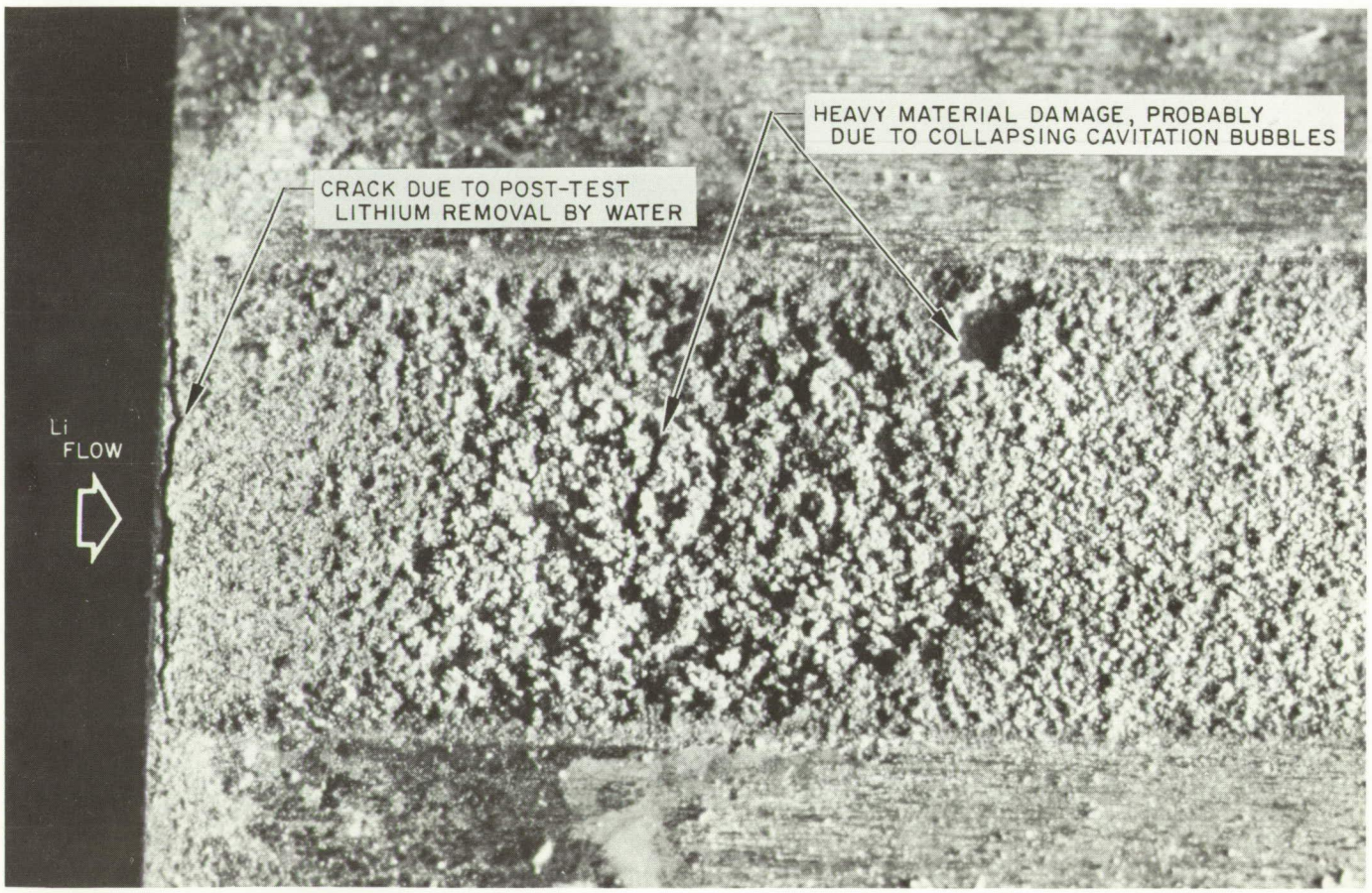

Fig. B-6. Cavitation damage of flow channel surface at test section exit

II. Test Section

The most severe damage observed on the test specimens was downstream of a void left by the dissolved yttria at the location of the highest velocity. Figure B-6 is a photograph of the damaged plate. The damage probably resulted from the collapse of cavitation bubbles or wakes resulting from the step change in cross section. Other investigators have noted the poor resistance of Nb-1%Zr to cavitation damage. Figure B-7 is a cross section of one of the craters at this location.

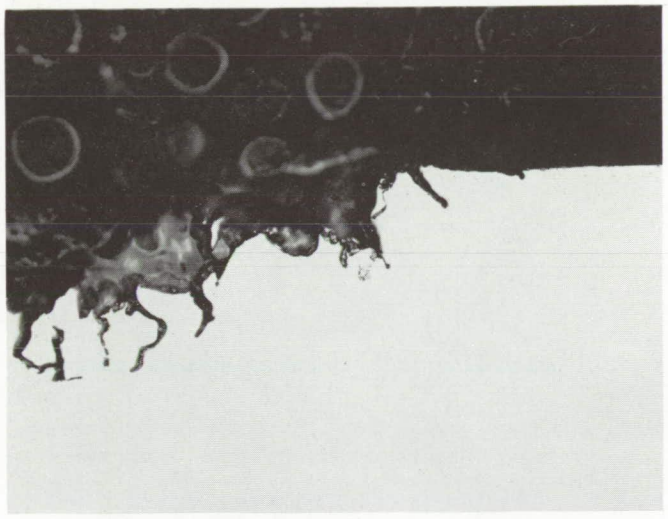

Fig. B-7. Section showing cavitation pit at test section exit (200 ×) (Photo reduced to 75%)

The appearance of the surfaces exposed to high-velocity lithium was different from adjacent unexposed portions. Figure B-8 shows cross sections of the surface at both locations. Surfaces adjacent to the flow channel that were exposed to seepage showed a roughening similar to that of the primary flow surface but with less material loss. Figures B-9 and B-10 are photomicrographs of surfaces that were exposed to such seepage. Small yttrium deposits can be seen, together with the pronounced grooving of both the surface and the grain boundaries. These specimens had no metallurgical treatment prior to these photographs. The surface grooving has no preferred direction from grain to grain, showing that it is not the consequence of channeling erosion from the flow. Instead, it is thought to be preferential dissolution at the boundaries of crystal planes intersecting the surface. In Fig. B-10, some of the original grinding marks still remain on the surface.

Figures B-11 and B-12 are photomicrographs of the surface of the 48.5 m/s specimen at the same location. The former is focused on the Nb-1%Zr substrate and shows the grooving that occurred in the flow channel. The dark regions are yttrium crystals, which are out of the focal plane. The tops of these crystals are shown in Fig. B-12. As discussed in the text, these deposits were formed after the test as the flowing lithium was cooled. The measured surface roughness due to the crystals and the average crystal height are plotted versus velocity in Fig. B-13. The measured points exhibit a dependence on velocity to the 0.8 power, indicating that the deposition process was diffusion limited.

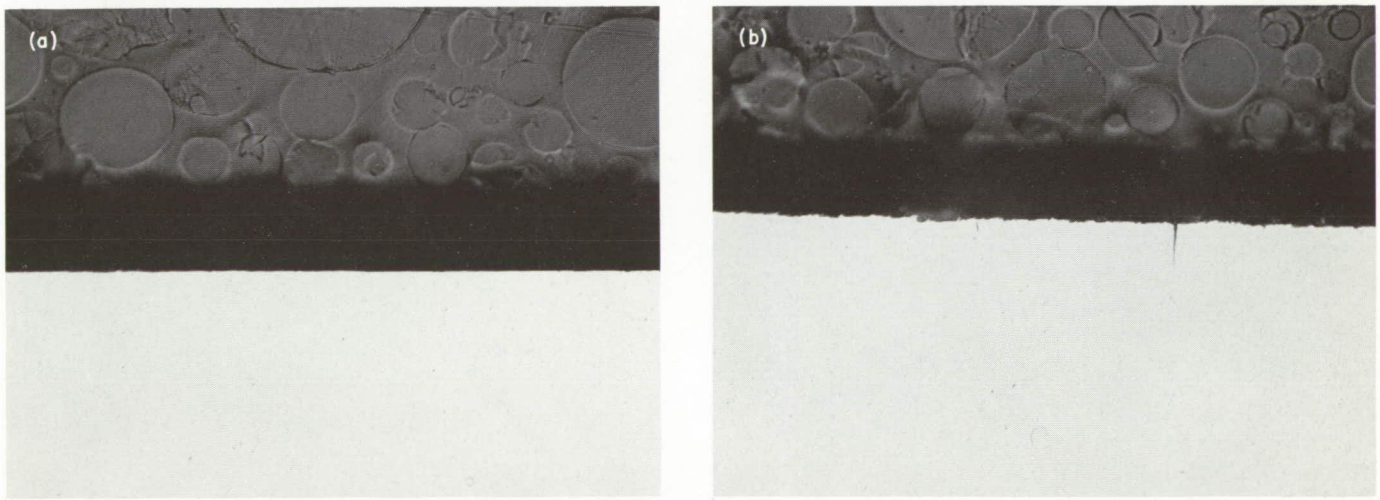

Fig. B-8. Section of surface after 500 hr at 1073–1143°C (100 ×) (Photo reduced to 75%)
(a) Surface adjacent to 48.5 m/s flow channel (b) Surface in 48.5 m/s flow channel

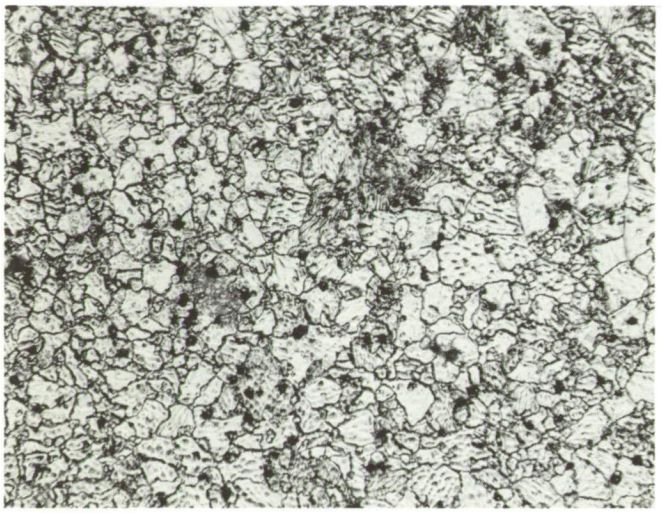

Fig. B-9. Surface exposed to lithium seepage, first location (250 ×) (Photo reduced to 75%)

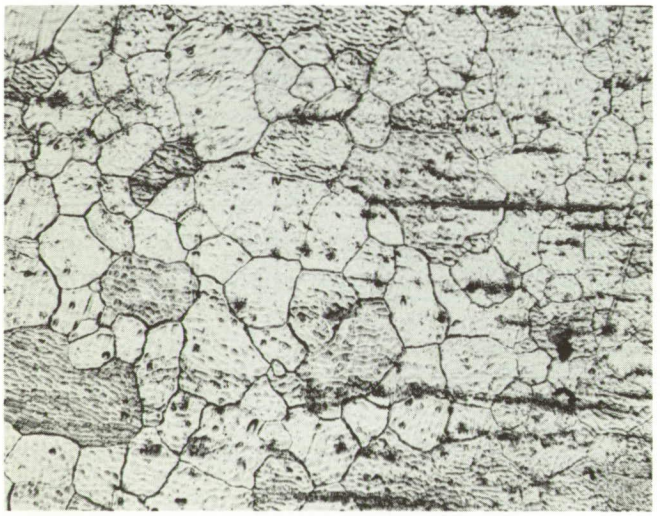

Fig. B-10. Surface exposed to lithium seepage, second location (250 ×) (Photo reduced to 75%)

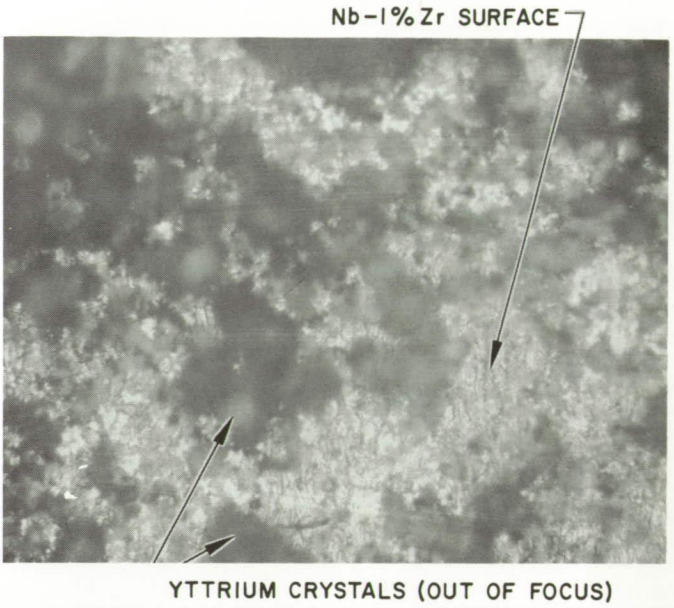

Fig. B-11. Surface of 48.5 m/s flow channel (250 ×) (Photo reduced to 82%)

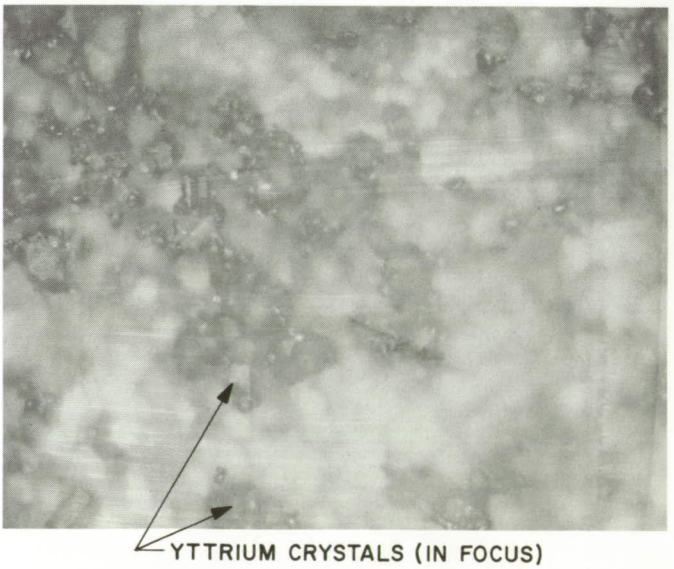

Fig. B-12. Crystals of yttrium deposited on surface of 48.5 m/s flow channel (250 ×) (Photo reduced to 82%)

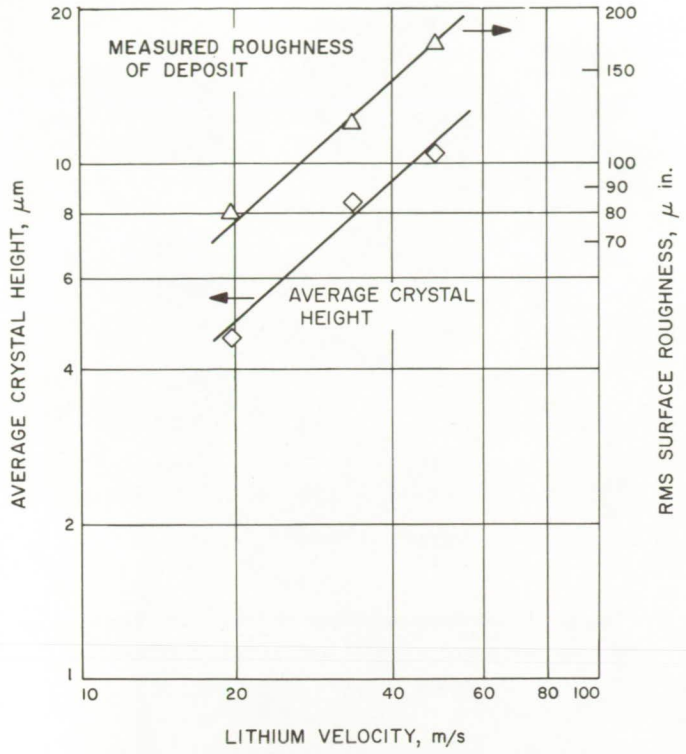

Fig. B-13. Yttrium crystal height and surface roughness vs lithium velocity

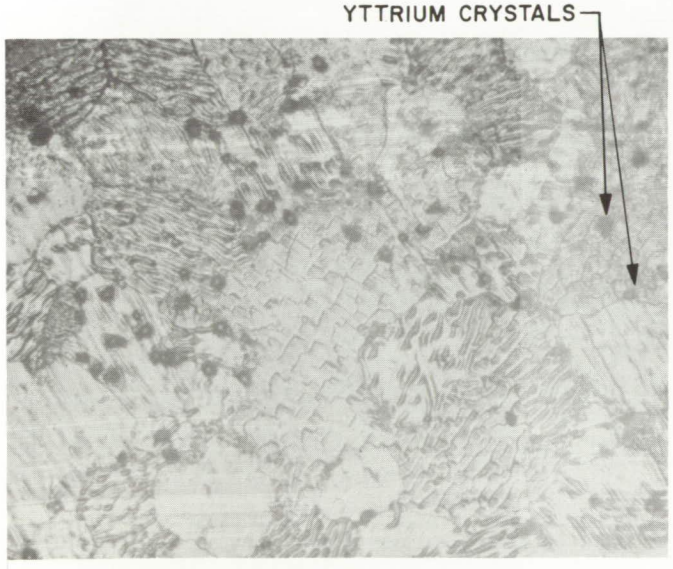

Fig. B-14. Surface adjacent to 48.5 m/s flow channel (250 ×) (Photo reduced to 82%)

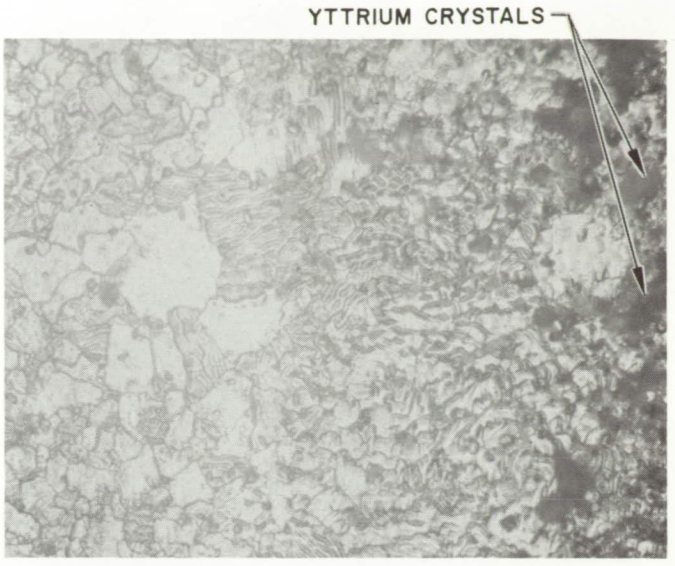

Fig. B-15. Surface at boundary of 48.5 m/s flow channel (250 ×) (Photo reduced to 82%)

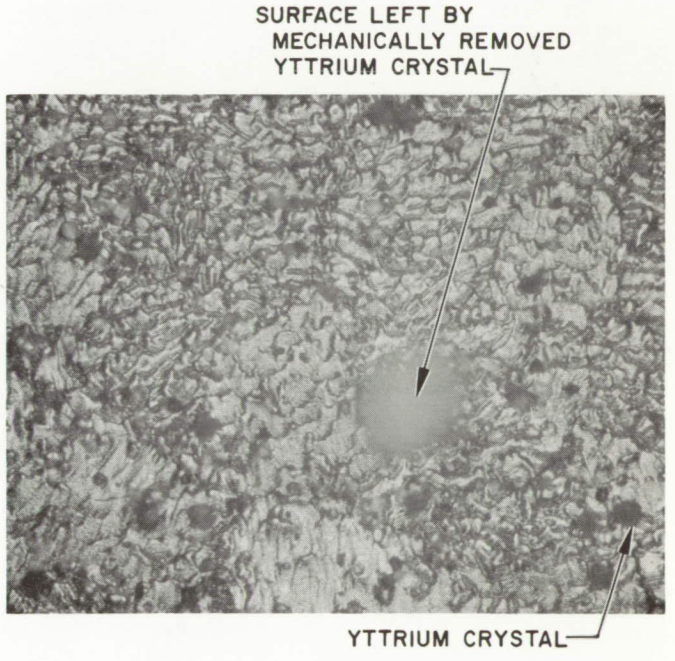

Fig. B-16. Surface of 19.6 m/s flow channel, first location (250×) (Photo reduced to 82%)

Figures B-14 through B-18 are additional photomicrographs of surfaces adjacent to and within the flow channel. All of these photographs show the grooving previously discussed. Careful examination of these figures shows the grooving to be continuous underneath crystals and in places where the crystals were mechanically removed (see Fig. B-18). This observation established that the crystals were formed after the high-temperature, high-velocity portion of the tests were completed during the cooling period.

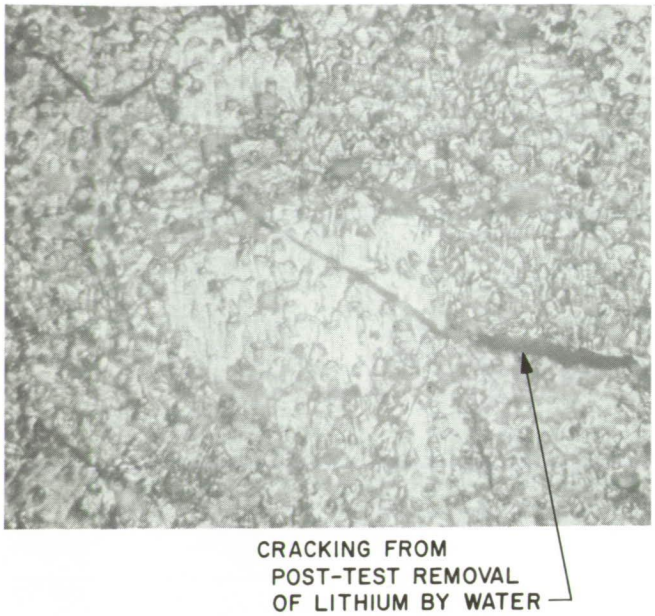

Fig. B-17. Surface of 19.6 m/s flow channel, second location (250 ×) (Photo reduced to 82%)

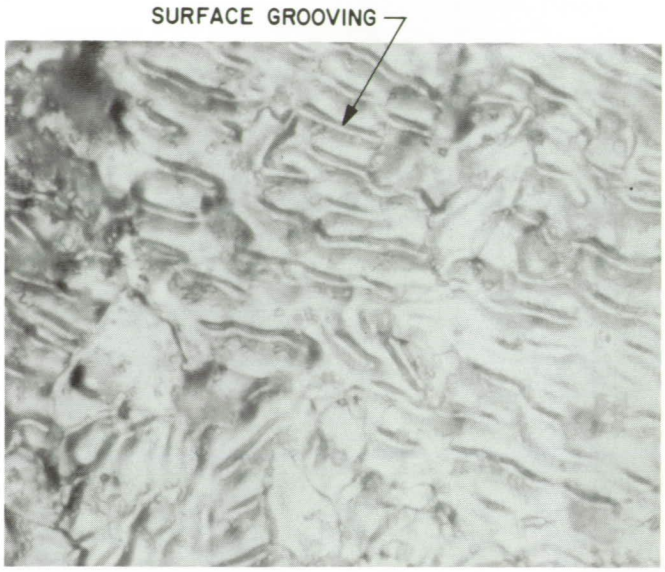

Fig. B-18. Surface adjacent to 48.5 m/s channel showing grooving of grain faces (750 ×) (Photo reduced to 82%)

Appendix C
Calculation of Material Removal

The basic mass-transfer relation for flow in a channel of constant cross is

$$d\dot{m}_w = \dot{m}_w P\,dx = \rho_s k_d (C_w - C_s) P\,dx \qquad \text{(C-1)}$$

The change in stream concentration dC_s over the interval dx, is just $d\dot{m}_w/\dot{m}_s$. Substitution and integration over the interval i, e of constant wall temperature gives

$$\ln \frac{C_w - C_{se}}{C_w - C_{si}} = -k_d \rho_s A_{i,e}/\dot{m}_s \qquad \text{(C-2)}$$

where the subscripts i and e apply to the entrance and exit of the interval i, e, and $A_{i,e}$ = total wall area in the interval i, e.

If the change in concentration $\Delta C_{si,e}$ over this interval is used, then Eq. (C-2) can be rearranged to give

$$\Delta C_{si,e} = (C_w - C_{si})(1 - e^{-k_d \rho_s A_{i,e}/\dot{m}_s}) \qquad \text{(C-3)}$$

Expressing the stream and wall concentrations in terms of the solubility S and the effective concentration temperature T_c gives

$$\Delta C_{si,e} \approx \left.\frac{\partial S}{\partial T}\right|_{T_{ci}} (T_{ce} - T_{ci}) \qquad \text{(C-4)}$$

$$C_w - C_{si} = \left.\frac{\partial S}{\partial T}\right|_{T_{ci}} (T_w - T_{ci}) \qquad \text{(C-5)}$$

Therefore,

$$\Delta T_{ce,i} \approx (T_w - T_{ci})(1 - e^{-k_d \rho_s A_{i,e}/\dot{m}_s}) \qquad \text{(C-6)}$$

This relation is independent of the magnitude of the solubility and can be applied independently. For fully developed flow, k_d is determined from the following relations:

$$Sh = 0.023\, Re^{0.8}\, Sc^{0.33} \qquad \text{(C-7)}$$

$$Sh = \frac{k_d d_h}{D_v} \qquad \text{(C-8)}$$

$$Re = \frac{V_s d_h}{\nu_s} \qquad \text{(C-9)}$$

$$Sc = \frac{\nu_s}{D_v} \qquad \text{(C-10)}$$

If the effective stream concentration temperature at the location of interest is known, then the thickness of material lost from the wall is seen to be:

$$\Delta t_w = k_d \frac{\rho_s}{\rho_w} \left.\frac{\partial S}{\partial T}\right|_{T_w} (T_w - T_c)\,\tau \qquad \text{(C-11)}$$

To compute Δt_w at the exit of each interval of the test section, the effective concentration temperature must be known at that location. To accomplish this the temperature distribution throughout the loop was calculated. Next, k_d was computed for each constant flow area section [from Eqs. (C-7) through (C-10)]. For sections with a constant wall temperature, Eq. (C-6) can then be applied directly to calculate the change in the effective concentration temperature. Sections with slowly varying wall temperatures (due to radiative losses or pump power input) were further subdivided into 10 increments, and the average wall temperature in each was used in Eq. (C-6).

A schematic of the test loop and the location of the measured temperature is shown in Fig. C-1. For each test period T_τ was measured by an optical pyrometer. Test period A was 109-hr duration at 1143°C. Period B was 391-hr duration at 1073°C. The loop temperatures and mass transfer were calculated for each period separately. Lithium properties at the time average temperature of 1088°C were used.

Period A

For the duration of this test period, the average lithium flowrate was 0.202 kg/s. The reservoir level was about 4.3 cm below the top. The reservoir cylindrical surface was grit-blasted, giving an effective emissivity at 1143°C of 0.32 (Ref. A-2). The top and bottom surfaces were as-received niobium plate having an emissivity of 0.295. Assumption of a view factor of unity leads to the following relation for heat loss from the reservoir:

$$Q_r = (\epsilon_C \sigma A_C + \epsilon_e \sigma A_e)(T_\tau^4 - T_a^4) \qquad \text{(C-12)}$$

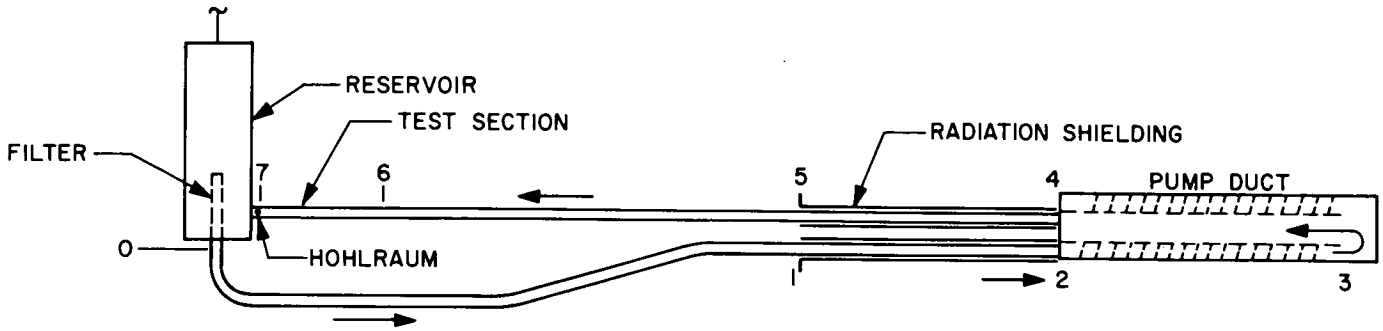

SECTION NO.	DEVELOPED LENGTH	OUTSIDE DIAM	HYDRAULIC DIAM	WETTED AREA
0,1	103.0 cm	2.54 cm	1.905 cm	616 cm^2
1,2	66.0	2.54	1.905	395
2,3	795.0	—	1.278	4240
3,4	45.7	5.43	4.370	626
4,5	66.0	2.54	1.905	395
5,6	74.2	2.54	1.905	444
6,7	17.8	2.54	—	—
RESERVOIR	34.3	8.89	8.25	888

Fig. C-1. Schematic of test loop geometry and station numbers

Substitution of the proper numbers for this period of the test gives:

$$Q_r = [(0.32)(1.354)(837) + (0.295)(1.354)(62.0)] \times [(1.416)^4 - (0.533)^4]$$
$$= 1529 \text{ cal/s}$$

From the heat rejected T_0 can be calculated:

$$T_0 = T_7 - \frac{Q_r}{\dot{m}_s c_{p_s}} \qquad \text{(C-13)}$$

$$= 1143 - \frac{1529}{(202)(1.0)} = 1143 - 7.57 = 1135°\text{C}$$

The heat radiated from 0 to 1 is approximately

$$Q_{0,1} = \epsilon_{0,1}\,\sigma A_{0,1}(T_0^4 - T_a^4) \qquad \text{(C-14)}$$
$$= [(0.295)(1.354)(822)][(1.408)^4 - (0.533)^4]$$
$$= 1270 \text{ cal/s}$$

The temperature T_1 is given by:

$$T_1 = T_0 - \frac{Q_{0,1}}{\dot{m}_s c_{p_s}} \qquad \text{(C-15)}$$

The section 1, 2 is insulated with 20 layers of dimpled foil so that the temperature T_2 is very nearly equal to T_1.

The heat loss from section 5, 7 is calculated next so that the total heat input can be related to the summation of the three losses. The relation for this heat loss $Q_{5,7}$ is given by:

$$Q_{5,7} = \epsilon_{5,7}\,\sigma A_{5,7}(T_7^4 - T_a^4) \qquad \text{(C-16)}$$
$$= (0.295)(1.354)(733)[(1.416)^4 - (0.533)^4]$$
$$= 1153 \text{ cal/s}$$

The temperature $T_5 = T_4$ is given by

$$T_5 = T_7 + \frac{Q_{5,7}}{\dot{m}_s c_{p_s}} \qquad \text{(C-17)}$$

$$= 1143 + \frac{(1153)}{(202)(1.0)} = 1143 + 5.72 = 1149°\text{C}$$

The temperature T_6 can be obtained by the ratio of length of the 6, 7 section to the total 5, 7 section.

$$\frac{T_7 - T_6}{T_7 - T_5} = \frac{17.8}{92.0} = 0.1937$$

$$T_7 - T_6 = (0.1937)(5.72) = 1.1°\text{C}$$

Therefore,

$$T_6 = 1144°C$$

The total heat input to the lithium is

$$Q_i = Q_r + Q_{0,1} + Q_{5,7} = \frac{(1529 + 1270 + 1153)(4.185)}{1000} = 16.55\,\text{kW} \tag{C-18}$$

The largest part of this heat is added to the lithium in the outer annulus of the pump, so

$$T_3 = T_2 + \frac{Q_i}{\dot{m}_s c_p} = 1129 + \frac{(3952)}{(202)(1.0)} = 1129 + 19.5 = 1149°C$$

The values used for constants of Eq. (C-7) through (C-11) were

$$\mu_s = 0.150 \text{ centipoise}$$
$$\rho_s = 0.434 \text{ g/cm}^3$$
$$\rho_w = 8.39 \text{ g/cm}^3$$
$$D_v = 4.1 \times 10^{-4} \text{ cm}^2/\text{s [from Eq. (4)]}$$

Application of these values to Eqs. (C-7) through (C-10) and the geometry of Fig. C-1 gives

Loop section	Re	Sh	k_d	$\Delta T_{ci,e}$	$\Sigma\Delta T_{ci,e}$
0, 1	0.93×10^5	442	0.0947	−0.447	−0.447
1, 2	0.93×10^5	442	0.0947	−0.574	−1.021
2, 3	1.04×10^5	485	0.155	+5.03	+4.01
3, 4	0.41×10^5	228	0.0213	+0.26	+4.27
4, 5	0.93×10^5	442	0.0947	+0.88	+5.15
5, 6	0.93×10^5	442	0.0947	+0.58	+5.73

The results mean that the effective concentration temperature at the inlet to the test section has increased by 5.73°C above the value at the reservoir exit. The concentration changes slightly within the test section itself. The following were calculated for each section of the test channel from Eqs. (C-7) through (C-10) and Eq. (C-11), using a value of $\partial S/\partial T|_{T_w} = 1.2 \times 10^{-9}\ °C^{-1}$ and $\tau = 109$ hr.

Section of test channel	$A_{i,e}$	k_d	$T_{we} - T_7$	$T_{ce} - T_7$	Δt_w, μm (for exit)
1	13.12	0.748	0.69	−1.78	0.42
2	8.35	1.40	0.32	−1.72	0.70
3	5.98	2.02	0	−1.67	0.80

Period B

During period B the lithium level was at the top of the reservoir. The measured temperature was $T_7 = 1073°C$.

Substitution in Eq. (C-12) gives

$$Q_r = [(0.32)(1.354)(957)] + [(0.295)(1.354)(124.0)][(1.346)^4 - (0.533)^4]$$
$$= 1488 \text{ cal/s}$$

The average flowrate for this period was also 202 g/s. Thus T_0 is given by

$$T_0 = T_7 - \frac{1488}{(202)(1.0)} = 1073 - 7.37 = 1067°C$$

The heat radiated from 0 to 1 is

$$Q_{0,1} = [(0.295)(1.354)(822)][(1.340)^4 - (0.533)^4]$$
$$= 1030 \text{ cal/s}$$

and

$$T_1 = T_2 = 1067 - \frac{1030}{(202)(1.0)} = 1067 - 5.10 = 1061°C$$

$$Q_{5,7} = [(0.295)(1.354)(733)][(1.346)^4 - (0.533)^4]$$
$$= 938 \text{ cal/s}$$

$$T_5 = T_7 + \frac{938}{(202)(1.0)} = 1073 + 4.64 = 1078°C$$

$$T_6 = T_7 + [(0.1937)(4.64)] = 1073 + 0.900 = 1074°C$$

$$Q_i = \frac{(1488 + 1030 + 938)}{1000} 4.185 = 14.48 \text{ kW}$$

$$T_3 = T_2 + \Delta T_r + \Delta T_{0,1} + \Delta T_{5,7}$$
$$= 1067 + 7.37 + 5.10 + 4.64 = 1067 + 17.11$$
$$= 1084°C$$

Application of these values to Eqs. (C-7) through (C-10) gives

Loop section	$\Sigma T_{ci,e}$	$\Sigma \Delta T_{ci,e}$
0, 1	−0.36	−0.36
1, 2	−0.47	−0.83
2, 3	+3.33	+2.50
3, 4	+0.19	+2.69
4, 5	+0.63	+3.32
5, 6	+0.39	+3.71

Use of this value of the change in effective concentration temperature in Eqs. (C-7) through (C-10) and Eq. (C-11) gives

Section of test channel	$T_{we} - T_7$	$T_{ce} - T_7$	Δt_w, μm (for exit)
1	0.567	−3.47	2.6
2	0.265	−3.37	4.4
3	0	−3.28	5.7

The total predicted material loss is the sum of periods A and B

Section of test channel	Total material loss, μm
1	3.0
2	5.1
3	6.5

Nomenclature

$A_{i,e}$ surface area of channel or piping between stations i and e, cm²

A_C area of reservoir cylindrical surface to lithium level, cm²

A_e area of reservoir ends exposed to lithium, cm²

C concentration of solute in solvent, by weight

c_p specific heat of solvent, cal/g

d_h hydraulic diameter, cm

D_v diffusivity of solute in solvent, cm²/s

k Boltzmann constant

k_d mass-transfer coefficient, cm/s

$\dot{m}_w$ mass-transfer rate per unit area from wall, g/cm²s

$\dot{m}_s$ mass flowrate of solvent (stream), g/s

r_a atomic radius of solute at melting point, cm

P perimeter of channel, cm

Re Reynolds number $= Vd_h/\nu$

Q_r heat rejected from reservoir, cal/s

S equilibrium solubility of solute in solvent, by weight

Sc Schmidt number $= \nu/D_v$

Sh Sherwood number $= k_d d_h/D_v$

T temperature, °C, °K

T_c effective concentration temperature, °C

Δt_w total thickness of material lost from wall for a period τ, cm

V velocity of solvent, cm/s

x length of channel, cm

ϵ_C emissivity of reservoir cylindrical surface

ϵ_e emissivity of reservoir ends

$\epsilon_{i,e}$ surface emissivity of piping section between stations i and e

μ viscosity of solvent, poise

ν kinematic viscosity of solvent, cm²/s

ρ_s density of solvent, g/cm³

ρ_w density of wall, g/cm³

τ time period over which Δt_w is measured, s

Subscripts

a ambient

e end point of interval of channel

i initial point of interval of channel

i, e; 1, 2; etc. values for interval of channel lying between end points i and e, 1 and 2, etc. (see Fig. C-1)

s value in stream (bulk)

w value at wall

1, 2, 3, etc. station number (see Fig. C-1)

References

1. Dunn, W. E., Bonilla, C. F., et al., "Mass Transfer in Liquid Metals," *A.I.Ch.E. J.*, Vol. 2, pp. 184–189, June, 1956.

2. Bonilla, C. F., "Mechanisms in Liquid Phase Corrosion, Diffusion Controlled," *Proc. of the NASA-AEC Liquid Metals Corrosion Meeting, Vol. I*, pp. 35–42, NASA SP-41, 1964.

3. Overman, A. Y., et al., *LCRE Non-nuclear Systems Test*, Final Report PWAC-402, Part IV, Pratt & Whitney Aircraft, Middletown, Conn., Oct.,1965.

4. Elliott, D., Cerini, D., and Hays, L., "Liquid Magnetohydrodynamic Power Conversion," *Supporting Research and Advanced Development*, Space Programs Summary 37-41, Vol. IV, pp. 124–132, Jet Propulsion Laboratory, Pasadena, Calif., Oct., 1966.

5. McKisson, R., et al., *Solubility Studies of Ultra Pure Transition Elements in Ultra Pure Alkali Metals*, Report AI-65-210, Atomics International, Canoga Park, Calif., Mar., 1966.

A-1. Hays, L., and O'Connor, D., *A 2000°F Lithium Erosion and Component Performance Experiment*, Technical Report 32-1150, Jet Propulsion Laboratory, Pasadena, Calif., Oct. 1, 1967.

A-2. Huttinger, R., *Determination of the Emissivity of Materials*, Report PWA-2206, Vol. III, Pratt & Whitney Aircraft, East Hartford, Conn., 1963.

B-1. Sessions, C., "Corrosion of Advanced Refractory Alloys in Lithium," *Proceedings of the AEC-NASA Liquid Metals Information Meeting*, pp. 143–148, AEC Report CONF-650411, April, 1965.